Applied Radiation and Isotopes 202 (2023) 111044

Contents lists available at ScienceDirect

Applied Radiation and Isotopes

journal homepage: www.elsevier.com/locate/apradiso

Determination of the Terbium-152 half-life from mass-separated samples from CERN-ISOLDE and assessment of the radionuclide purity

S.M. Collins [a,b,*], U. Köster [c], A.P. Robinson [a,d,e], P. Ivanov [a], T.E. Cocolios [f], B. Russell [a], A.J. Fenwick [a], C. Bernerd [f,g], S. Stegemann [f], K. Johnston [g], A.M. Gerami [g], K. Chrysalidis [g], H. Mohamud [a], N. Ramirez [a], A. Bhaisare [a], J. Mewburn-Crook [a], D.M. Cullen [e], B. Pietras [e], S. Pells [e], K. Dockx [f], N. Stucki [h], P.H. Regan [a,b]

[a] National Physical Laboratory, Hampton Road, Teddington, TW11 0LW, UK
[b] School of Mathematics and Physics, University of Surrey, Guildford, GU2 7XH, UK
[c] Institut Laue-Langevin, 38042, Grenoble, France
[d] Christie Medical Physics and Engineering (CMPE), The Christie NHS Foundation Trust, Manchester, M20 4BX, UK
[e] The University of Manchester, Manchester, M13 9PL, UK
[f] KU Leuven, Institute for Nuclear and Radiation Physics, Celestijnenlaan 200D, 3001, Leuven, Belgium
[g] CERN – European Organization for Nuclear Research, Esplanade des Particules 1, 1217, Meyrin, Switzerland
[h] HEPIA, HES-SO, University of Applied Sciences and Arts Western Switzerland, Rue de la Prairie 4, 1202, Geneva, Switzerland

A B S T R A C T

Terbium-152 is one of four terbium radioisotopes that together form a potential theranostic toolbox for the personalised treatment of tumours. As ^{152}Tb decay by positron emission it can be utilised for diagnostics by positron emission tomography. For use in radiopharmaceuticals and for activity measurements by an activity calibrator a high radionuclide purity of the material and an accurate and precise knowledge of the half-life is required. Mass-separation and radiochemical purification provide a production route of high purity ^{152}Tb. In the current work, two mass-separated samples from the CERN-ISOLDE facility have been assayed at the National Physical Laboratory to investigate the radionuclide purity. These samples have been used to perform four measurements of the half-life by three independent techniques: high-purity germanium gamma-ray spectrometry, ionisation chamber measurements and liquid scintillation counting. From the four measurement campaigns a half-life of 17.8784(95) h has been determined. The reported half-life shows a significant difference to the currently evaluated half-life (ζ-score = 3.77), with a relative difference of 2.2 % and an order of magnitude improvement in the precision. This work also shows that under controlled conditions the combination of mass-separation and radiochemical separation can provide high-purity ^{152}Tb.

1. Introduction

Terbium-152 (Q(ε) = 3.99(4) MeV) undergoes radioactive decay via the competing processes of electron capture (I_ε = 83 %) and positron emission ($I_{\beta+}$ = 17 %) from the ground state ($I^\pi = 2^-$; $T_{1/2}$ = 17.5(1) h). In the cases of decays to excited states in the daughter nucleus, these weak interactions are followed by subsequent de-excitations via electromagnetic transitions to the ground state of the stable ^{152}Gd (Martin, 2013). Direct ground state to ground state decay occurs with an approximate 25 % probability, with the remaining decay pathways navigating through a total of 111 proposed excited states of the daughter nuclei. There are currently over 200 gamma transitions identified from decays between these states. Of these transitions, there are only a few that result in a gamma-ray emission with a significant intensity ($I_\gamma > 1$ %) and at a suitable energy for possible interest in medical imaging applications.

It is the presence of the positron decay branch, coupled with its relatively short half-life, that makes the ^{152}Tb an interesting candidate for diagnostic positron emission tomography (PET). Recent in-vivo PET imaging studies have shown reasonable PET imaging performance, though spatial resolution can be poor due to the relatively high positron energy and interfering gamma rays (Müller et al., 2012, 2016). In these studies, some advantages were identified over other PET radioisotopes, such as ^{68}Ga ($T_{1/2}$ = 67.83(20) min (Kuzmenko, 2019)), due to the possibility of longer imaging periods and potentially preferable to ^{89}Zr ($T_{1/2}$ = 78.361(25) h (Fenwick et al., 2020)) or ^{64}Cu ($T_{1/2}$ = 12.7004 (20) h (Bé et al., 2011)) due to chemistry constraints requiring different chelators for coordination with existing radiotherapeutic radionuclides such as ^{177}Lu and ^{166}Ho. First in-human PET/CT studies of ^{152}Tb-DOTATOC and ^{152}Tb-PSMA have been reported for neuroendocrine tumours and prostate cancer, respectively (Baum et al., 2017; Müller et al.,

* Corresponding author. National Physical Laboratory, Hampton Road, Teddington, TW11 0LW, UK.
E-mail address: sean.collins@npl.co.uk (S.M. Collins).

https://doi.org/10.1016/j.apradiso.2023.111044
Received 28 July 2023; Received in revised form 15 September 2023; Accepted 22 September 2023
Available online 27 September 2023

2019).

A member of the unique terbium radioisotope quartet (^{149,152,155,161}Tb) for molecular radiotherapy and diagnosis, ^{152}Tb can be used as the complimentary diagnostic element of a possible theranostic pair, e.g. ^{149}Tb/^{152}Tb (Müller et al., 2012, 2014). The identical chemical characteristics and suitable physical half-lives of these radioisotopes present an advantageous system for molecular radiotherapy. Utilising the same targeting vector provides the capability for unique theranostic treatment strategies and facilitates their application in personalised medicine (Müller et al., 2012).

Before this radionuclide can be implemented routinely in a clinical setting, the activity of the radionuclide must be determined via a radionuclide calibrator which is traceable to a primary standard for the activity of ^{152}Tb (Zimmerman and Judge, 2007). The relative standard uncertainty ($u(T_{1/2})/T_{1/2} = 0.57$ %) of the current evaluated half-life of ^{152}Tb is incompatible with precision activity measurements, such as would be needed for a primary standardisation. At the time of the present work there have been only two reported determinations of the half-life, both of which were published in the 1960s, with values of 17.4 (3) h and 17.5(1) h (Toth et al., 1960; Gromov et al., 1967). These previous investigations have made use of mass separated and radiochemically purified sources of ^{152}Tb but lack any details of the remaining contaminants. There is also a common lack of detail in the publications and any serious analysis of the uncertainty components. Recent studies of ^{155}Tb and ^{161}Tb have shown that the half-lives reported in previous measurements of these terbium radioisotopes have been of limited accuracy (Durán et al., 2020; Collins et al., 2022a, 2022b; Dong et al., 2023). It is therefore of importance to determine this half-life with more precision than currently available in the literature and to confirm the accuracy of the previous measurements.

In the current work, we have studied the ratio of gamma-ray emitting contaminants identified in two mass separated samples of ^{152}Tb, from CERN-ISOLDE in 2018 and 2022, by high-purity germanium (HPGe) gamma-ray spectrometry to provide an indication of the purification achievable by mass-separation and with additional radiochemical purification. These samples have also been used to determine the half-life of ^{152}Tb by three radiometric techniques: liquid scintillation counting (LSC), ionisation chamber measurements (IC) and HPGe gamma-ray spectrometry. All uncertainties are stated as standard uncertainties or combined standard uncertainties as defined in the *Guide to the Expression of Uncertainty in Measurement* (GUM) (BIPM, 2008).

2. Methodology and results

2.1. Production and mass-separation

Mass-separated ^{152}Tb samples were produced, by the collection and resulting decay of the precursor ^{152}Dy ($T_{1/2} = 2.38(2)$ h (Martin, 2013)), at the CERN-ISOLDE facility during the formal experiments IS528 (2018) and IS688 (2022). A beam of 1.4 GeV protons from the CERN Proton Synchrotron Booster induced nuclear reactions in a 94 g cm^{-2} high purity Ta foil target (as rolls of 6 μm and 20 μm thick foils). The produced radiogenic nuclides were on-line released from the 2000 °C hot target and thermally ionised in an adjacent 2000 °C hot tungsten tube, electrostatically accelerated to 30 keV, mass-separated at A = 152 by deflection in the magnetic dipole of the ISOLDE General Purpose Separator and ion-implanted at 30 keV into a Zn-coated Au foil in a vacuum chamber at the GLM, in 2018, and GHM, in 2022, beam lines (Catherall et al., 2017). To enhance the ionisation of ^{152}Dy, the radioactive precursor of ^{152}Tb, the resonance ionisation laser ion source was employed and tuned to ionise dysprosium (Köster et al., 2003; Rothe et al., 2011). The implantations were performed on June 26, 2018 for 127 min and on March 28, 2022 for 145 min at an average ion current of approximately 5 nA.

2.2. Sample 1 (2018)

2.2.1. Production and sample preparation

The collected sample was received at the National Physical Laboratory (NPL) on 28 June 2018 containing approximately 100 MBq of ^{152}Tb. The Zn coated Au foil was removed from the holder and the Zn layer dissolved in 20 mL of 6 M HCl for 2 h. The Au foil was removed and rinsed with 6 M HCl. The solution was evaporated to near-dryness before re-dissolving in 25 mL 0.1 M HCl with 10 μg g^{-1} stable Eu. No purification of the sample was performed.

From this resulting solution, a 9.6 g aliquot dispensed to a 10 mL ISO ampoule was prepared for measurement by ionisation chamber and a 1 g aliquot dispensed to a 2 mL ISO ampoule for measurement by HPGe gamma-ray spectrometry.

2.2.2. Activity assay and contaminants

Three sources of the ^{152}Tb solution were measured over the period from 28 June 2018 to 21 June 2021. The extended measurement campaign was to determine the activity of any long-lived radionuclide contaminants, such as ^{152}Eu ($T_{1/2} = 13.517(14)$ a (Bé et al., 2004)). The samples were measured with a 24 % relative efficiency HPGe gamma-ray spectrometer (identified as 'LOKI', previously described in detail in (Collins et al., 2022b)) with a source-to-detector distance of 295 mm ($\Omega/4\pi \sim 0.36$ %) to minimise true coincidence summing corrections. The HPGe gamma-ray spectrometer had previously had its full-energy peak (FEP) detection efficiency calibrated over the energy range 22 keV–1836 keV, using a suite of sources traceable to national standards.

The main FEPs of ^{152}Tb and the identified contaminants are annotated on the gamma-ray spectrum in Fig. 1. In addition to the expected characteristic gamma-ray emissions of ^{152}Tb, signatures for ^{151}Tb and ^{153}Tb were identified as well as the ^{134}Ce/^{134}La pair (from the collection of ^{134}Ce^{18}O; identified from the 604 keV gamma-ray emission from the decay of ^{134}La) and ^{152m}Eu ($T_{1/2} = 9.3116(13)$ h (Martin, 2013)). The later measurement in June 2021, where ^{152}Tb was no longer present, revealed the presence of ^{152}Eu and ^{153}Gd, the presence of ^{153}Gd results from the decay of ^{153}Tb. Whilst not detected, the presence of ^{151}Gd ($T_{1/2} = 123.9(10)$ d (Singh, 2009) is also assumed as a decay product of ^{151}Tb ($T_{1/2} = 17.609(14)$ h (Singh, 2009)).

The activities were determined using the half-lives, gamma-ray energies and emission intensities provided in Table 1. The activity of the ^{152}Tb and contaminants at the end of collection (EoC) time at CERN-ISOLDE are given in Table 2, along with the ratio of the contaminant activity and number of atoms to the ^{152}Tb. The number of atoms provides an indication of the magnitude of the low- and high-mass tailing of the mass-separation process. It is assumed that the activity of ^{153}Gd was close to zero at the end of collection and was generated as the ^{153}Tb decayed. This assumption was supported by the comparison of activity of ^{153}Gd measured in June 2021 ($A(t\text{-}t_0 = 1091$ d) $= 1.05(22)$ Bq g^{-1}) and from the activity derived from the ingrowth of ^{153}Gd using the ^{153}Tb activity at the EoC using the Bateman equation ($A(t\text{-}t_0 = 1091$ d) $= 1.26(11)$ Bq g^{-1}). The activities determined from both methods agree within the standard uncertainties. It is also assumed that ^{151}Gd was negligible at the EoC. Fig. 2 shows the ratio of the contaminants (excluding the negligible contributions of ^{152}Eu and the ingrowth of ^{151}Tb and ^{153}Tb) to the ^{152}Tb as a function of time from the EoC.

2.3. Sample 2 (2022)

2.3.1. Radiochemistry, and sample preparation

Two collection foils were received at NPL on 31 March 2022. Each foil was placed in 10 mL of 6 M HCl to dissolve the Zn layer. Once dissolved the solutions were evaporated down to incipient dryness before re-dissolving in 1 mL of 0.75 HNO_3. Each solution was dispensed to a 2 mL ISO ampoule and measured using HPGe gamma-ray spectrometry to determine the initial ^{152}Tb activity. The activities for each solution are

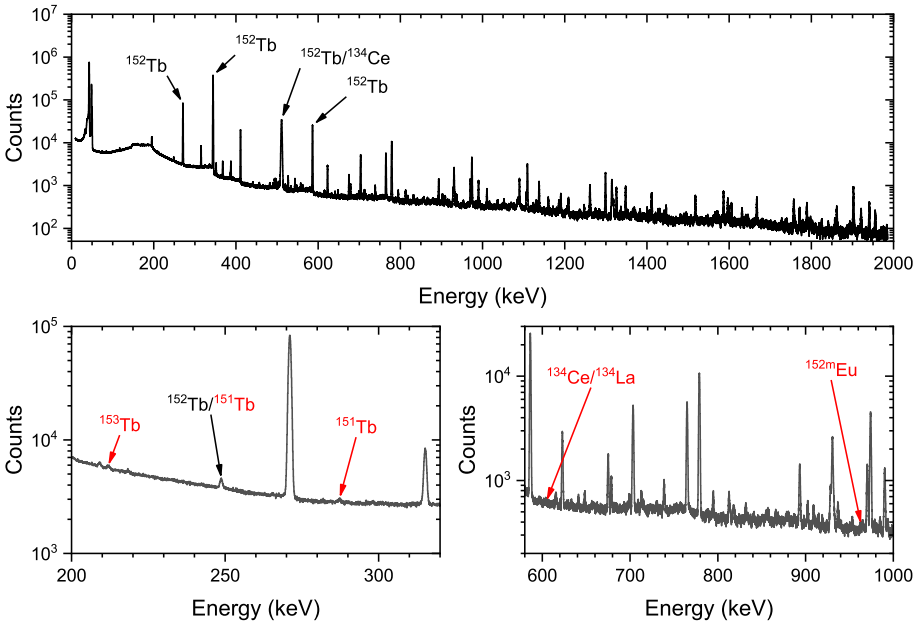

Fig. 1. Annotated gamma-ray spectrum following the decay of ^{152}Tb. The peaks used for the determination of the half-life are identified in the upper spectrum. The location of the contaminant full-energy peaks are identified in the zoomed in figures in the lower portion of this figure. The full-energy peaks of ^{134}La and ^{152m}Eu are too small to be seen in the figure.

Table 1
Half-lives and characteristic gamma-ray emissions used to determine the activity of each radionuclide identified in the samples.

Radionuclide	$T_{1/2}$	Gamma-ray energy (keV)	Gamma-ray emission intensity /100 decays	Reference
^{152}Tb	17.8784 (95) h	271.1 344.3 586.3 778.9 974.1 1109.2	9.53(21) 63.5(17) 9.21(21) 5.54(13) 2.997(70) 2.546(62)	(This work; Martin, 2013)
^{151}Tb	17.609 (14) h	287.4	28.3(12)	Singh (2009)
^{153}Tb	2.34(1) d	212.0	28.5(19)	Nica (2020)
^{155}Tb	5.2346 (36) d	86.6 105.3	30.71(25) 25.57(13)	(Webster, 2021; Collins et al., 2022b)
^{134}Ce–^{134}La	3.16(4) d	604.7 (^{134}La)	5.04(20)	Sonzogni (2004)
^{152m}Eu	9.3116 (13) h	963.4	11.7(18)	Martin (2013)
^{152}Eu	4938.8 (58) d	121.8	28.41(13)	Bé et al. (2004)
^{151}Gd	123.9(1) d	–	–	Singh (2009)
^{153}Gd	240.4 (10) d	97.4 103.1	30.15(20) 22.33(17)	(Bé et al., 2004; Shearman et al., 2017)

Table 2
Activity per unit mass of solution of the ^{152}Tb and contaminant radionuclides at the End of Collection time of 2018–06-26 09:28 UTC. The ratio of the contaminant radionuclide (Imp) activity and number of atoms (N_0) to that of ^{152}Tb is given.

Radionuclide	A_0 (kBq g^{-1})	A_0(Imp)/A_0(^{152}Tb)	N_0(Imp)/N_0(^{152}Tb)
^{152}Tb	2.998(41) × 10^4	–	–
^{151}Tb	14.9(19)	4.96(64) × 10^{-4}	4.96(63) × 10^{-4}
^{134}Ce–^{134}La	6.1(12)[a]	2.04(39) × 10^{-4}	8.6(17) × 10^{-4}
^{152m}Eu	4.8(19) × 10^2	1.60(62) × 10^{-2}	8.3(32) × 10^{-3}
^{152}Eu	6.98(42) × 10^{-3}	2.33(14) × 10^{-7}	1.54(14) × 10^{-3}

[a] Denotes the activity of the^{134}Ce determined from the^{134}La gamma-ray emission assuming that the parent-progeny are in equilibrium.

provided in Table 3. Following these measurements, each solution was radiochemically processed to remove Ce, Eu, and Gd from the solution following the procedure detailed in Webster et al. (2019). This resulted in two solutions of between 11 and 12 mL, 1 g aliquots of each solution were dispensed to 2 mL ISO ampoules and measured by HPGe gamma-ray spectrometry to determine the activity of ^{152}Tb recovered after processing. The activity recovered for each solution is given in Table 3 along with the recovery yield. The difference in the yield is likely due to the quantity of inactive Gd present, which can result in lower recovery yields (Webster et al., 2019). The remaining solution in both samples were combined and evaporated to incipient dryness and redissolved in 6.4 g of 0.1 M HCl containing 25 μg g^{-1} Gd. From this solution a 1 g aliquot was dispensed to a 2 mL ISO ampoule for measurement by HPGe gamma-ray spectrometry and 0.2 g aliquots were dispensed to two glass liquid scintillation vials containing 10 mL of Goldstar Quanta liquid scintillation cocktail for measurement by Triple-to-Double Coincidence Ratio (TDCR) counting.

2.3.2. Activity assay and contaminants

A single source of the radiochemically separated ^{152}Tb solution was measured over the period from 1 April 2022 to 22 April 2022. As with the 2018 sample, the extended measurement campaign was intended to identify the presence and determine the activity of any long-lived radionuclide contaminants. The initial measurements were performed at a 400 mm source-to-detector distance ($\Omega/4\pi \sim 0.128$ %) from a 9.5 % relative efficiency high-purity gamma-ray spectrometer (identified as 'THOR', previously described in detail in Collins et al. (2022b)). Later measurements were performed at a source-to-detector distance of 150 mm ($\Omega/4\pi \sim 0.888$ %). As with 'LOKI', the HPGe gamma-ray spectrometer 'THOR' had its FEP detection efficiency previously calibrated over the energy range 22 keV–1836 keV, using a suite of sources traceable to national standards.

Consistent with the sample received in 2018, the presence of ^{151}Tb and ^{153}Tb was identified along with their decay progeny of ^{151}Gd and

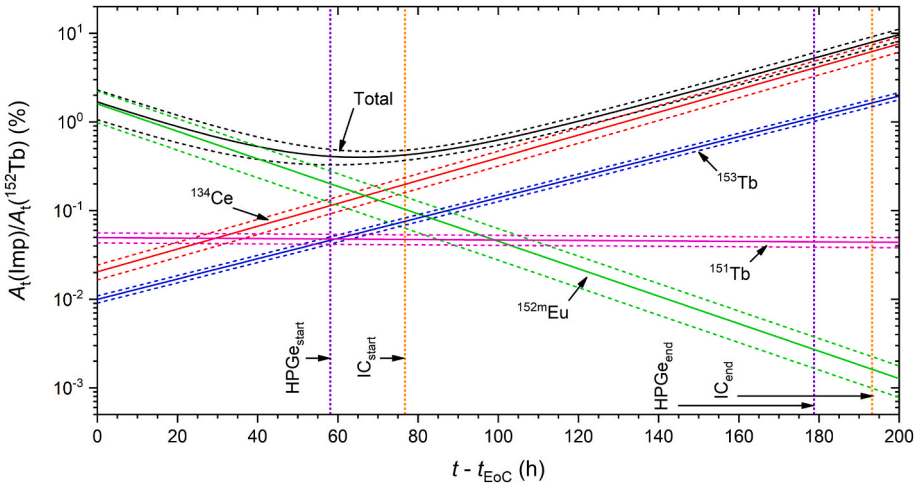

Fig. 2. Activity ratio of contaminants (Imp) to ^{152}Tb as a function of time starting from the EoC. The solid and dashed lines indicate the ratio and its standard uncertainty, respectively. The start and end of the half-life measurement campaigns for the HPGe gamma-ray spectrometry and Ionisation Chamber are shown by the vertical purple and orange dashed lines, respectively. (For interpretation of the references to colour in this figure legend, the reader is referred to the web version of this article.)

Table 3
Activity of ^{152}Tb recovered from the targets, the recovered activity after the radiochemical separation process and the yield. The activities are given at the reference time of 2022–03-28 22:40 UTC.

Target	Total activity recovered from Zn layer (MBq)	Total activity after Separation process (MBq)	Yield (%)
Zn/Au	37.7(13)	36.65(72)	97.2(39)
Zn/Pt	253.3(55)	203.5(39)	86.5(30)

^{153}Gd. However, unlike the 2018 sample, no presence of ^{134}Ce, ^{152m}Eu or ^{152}Eu was observed in the spectra. In the case of ^{152m}Eu, this is likely due to extended transport time from CERN to NPL and for ^{134}Ce and ^{152}Eu because of the radiochemical separation. However, the trace presence of ^{155}Tb and ^{139}Ce was identified. The presence of these radionuclides could potentially occur due to high mass tailing in the mass separation process but a simpler reason for its presence is due to a simultaneous collection of ^{152}Tb and ^{155}Tb at CERN-ISOLDE, which had resulted in cross-contamination of the sample foils. The activities at the end time of the chemical separation are presented in Table 4. As we can assume that the terbium isotopes would behave identically through the chemical separation process it can be assumed that the activity ratio of the contaminant terbium radioisotopes and the ratio of the number of atoms would remain the same even though the activity is lost during the radiochemical separation process. Table 4 presents the ratios of the activity of the terbium contaminants and the atom ratio at the EoC. The activity ratio of the ^{151}Tb and ^{153}Tb are approximately an order of magnitude greater than in 2018, the ratio of the mass-tailing of the ^{151}Tb from ^{153}Tb has also increased from 1.59 to 3.37. The evolution of the activity ratio of the terbium contaminants as a function of time commencing from the EoC is shown in Fig. 3.

2.4. Half-life determination

2.4.1. Ionisation chamber – sample 1

The 9.6 g aliquot of solution in a 10 mL ISO ampoule was held in a bespoke Perspex holder and measured in the NPL VINTEN 671 (SN: 3–5) secondary standard ionisation chamber (IC) using an in-house current measurement system. The campaign started on 29 June 2018 collecting a total of 4437 measurements in 4.85 d (approximately 6.5 half-lives of ^{152}Tb). The measurement times (Δt) were initially 21 s, increasing

Table 4
Activity per unit mass of solution and the activity ratio of the ^{152}Tb and contaminant radionuclides at the End of Separation (EoS) time of 2022–03-31 14:15 UTC. The activity ratios and atom ratios for the terbium contaminants (Imp) to ^{152}Tb are given at the End of Collection time of 2022–03-28 22:40 UTC. The detection limit (DL) for ^{134}Ce is also provided at the EoS.

Radionuclide	A_{EoS} (kBq g^{-1})	A_{EoS}(Imp)/A_{EoS}(^{152}Tb)	A_{EoC}(Imp)/A_{EoC}(^{152}Tb)	N_{EoC}(Imp)/N_{EoC}(^{152}Tb)
^{152}Tb	1.812(34) × 10^3	–		
^{151}Tb	17.0(11)	9.41(62) × 10^{-3}	9.90(64) × 10^{-3}	9.75(63) × 10^{-3}
^{153}Tb	8.83(62)	4.87(35) × 10^{-3}	9.21(66) × 10^{-4}	2.89(21) × 10^{-3}
^{155}Tb	1.140(19)	6.29(16) × 10^{-4}	7.70(17) × 10^{-5}	5.41(12) × 10^{-4}
^{139}Ce	1.49(74) × 10^{-3}	8.3(41) × 10^{-7}	–	–
^{134}Ce–^{134}La	DL = 0.51	DL = 2.83 × 10^{-4}		

gradually in duration over the campaign to 181 s. The IC and sample were not disturbed for the duration of the campaign. The sample provided a current of 204.58 pA in the first measurement and 2.3326 pA in the final measurement. An average background current, I_B, of 0.0386 pA was measured before the first measurement.

A weighted non-linear least-squares (WLS) fit to the dataset was performed, with additional terms to account for each of the contaminants observed, using:

$$I(t) = I_B + \sum \left(I_n \bullet e^{-\lambda_n t} \bullet \frac{1 - e^{-\lambda_n \Delta t}}{\lambda_n \Delta t} \right) \quad (1)$$

with the weight for each data point derived using:

$$\frac{\sigma(I)}{I} \approx \left[\frac{0.001}{I \bullet \Delta t} + \left(\frac{\sigma(I_B)}{I} \right)^2 \right]^{0.5} \quad (2)$$

where I_n is the response for each radionuclide in the solution, which have been identified as ^{151}Tb, ^{152}Tb, ^{153}Tb, ^{134}Ce, ^{152m}Eu, ^{152}Eu and ^{153}Gd, at $t = 0$, and λ_n are their respective decay constants, and t is the time elapsed since the reference time. The initial term in Eq. (2) is a general "rule of thumb" taken from an NPL technical procedure to provide an approximate relationship between the current measured over

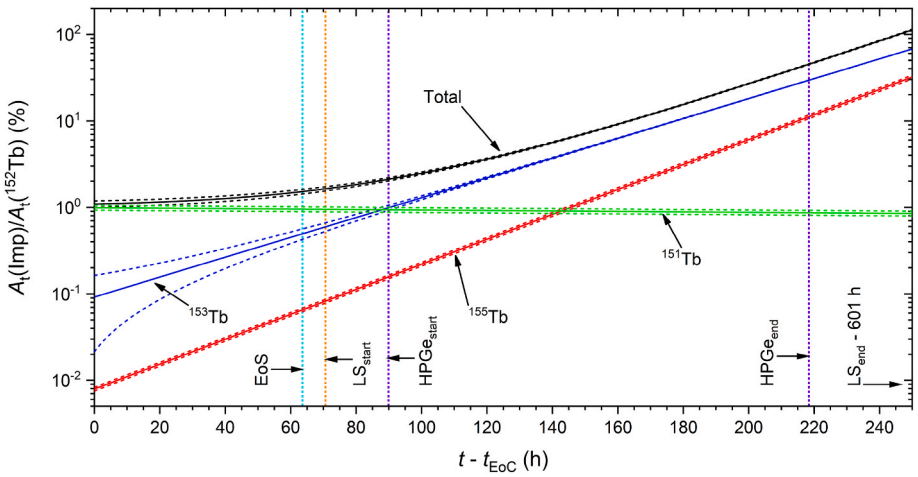

Fig. 3. Activity ratio of contaminants (Imp) to ^{152}Tb as a function of time starting from the EoC. The solid and dashed lines indicate the ratio and its standard uncertainty, respectively. The vertical dashed lines indicate the end time of the radiochemical separation process (pale blue), and the start and end of the half-life measurement campaigns for the HPGe gamma-ray spectrometry (purple) and liquid scintillation counting (orange). (For interpretation of the references to colour in this figure legend, the reader is referred to the web version of this article.)

a given time and its standard deviation. The value of 0.001 has been estimated empirically for this ionisation chamber. As the measurement time increased over the first 55.7 h, from 21 s to 181 s, similar currents were collected for each of these measurements and thus the weights derived from this term were approximately equivalent. Once the measurement time had reached its maximum of 181 s and the collected current started to reduce the standard deviation of the current measurement began to increase.

To improve the confidence of the fit, initial detection efficiencies (aka calibration factors (CF)) were modelled for each radionuclide, using the SIRIC modelling software (Cox et al., 2007), or existing factors used along with the activities in Table 2 to provide initial estimates of the *pA* for each radionuclide at $t = 0$. A SIRIC model for the 10 ml ISO ampoule was not available and therefore the modelling was performed using a geometry with 3 mL liquid in a 5 ml ISO ampoule. The factor for ^{152}Eu is derived from primary activity standards and is 3 mL liquid in a 5 ml BS ampoule. It is expected these differences will lead to discrepancies, particularly for beta (which includes ^{134}Ce/^{134}La) and low energy gamma emitting radionuclides. Furthermore, the model input parameters only cover energies from 30 keV to 1880 keV and therefore energies outside this range will be poorly modelled. Standard uncertainties stated relate to the non-linear least squares fit and the nuclear data used. The modelled CFs and their standard uncertainties are given in Table 5.

The WLS fit was performed where $I = A_0 \bullet CF$ for each radionuclide present, where A_0 is the activity of the radionuclide at the start time of the measurement campaign as determined by HPGe gamma-ray spectrometry and the CF is the modelled CF. The CF for all radionuclides, except ^{152}Eu, and the decay constant of the ^{152}Tb were free parameters, whilst the decay constants for all contaminants were fixed. By iterative refinement of the free parameters the maximum likelihood estimate of the half-life of ^{152}Tb was determined. The resulting CF determined from the WLS are provided in Table 5, where large relative differences of the modelled and WLS CFs for the contaminants are shown. Some of these sizable differences may be explained by factors previously outlined, however, the initial activity determined for the contaminants should also be considered. In Table 2, the activities for contaminants for this sample have imprecise relative standard uncertainties associated with them due to contributions from low statistics and the nuclear decay data. These standard relative uncertainties of the activities are typically the same magnitude as the differences observed in Table 5, and as such are not statistically significant different. The modelled decay rates for each radionuclide and residuals (as z-scores) of the fit (black diamonds) to the observed data are shown in Fig. 4, along with the residuals of the fit where only the presence of ^{152}Tb is considered (red diamonds).

Table 5
Table of modelled calibration factors of each radionuclide for the NPL VINTEN 671 secondary standard ionisation chamber compared to those determined from the weighted least-squares fit to the observed dataset.

Radionuclide	Calibration factor source	Modelled calibration factor(pA MBq^{-1})	WLS calibration factor(pA MBq^{-1})	(CF_{WLS}/ CF_{model})-1 (%)
^{152}Tb	SIRIC	13.99(27)	13.6957	−2.13
^{151}Tb	SIRIC	8.78(11)	10.3898	18.36
^{153}Tb	SIRIC	2.066(37)	1.8104	−12.38
^{134}Ce–^{134}La	SIRIC	7.352(75)	8.8733	20.69
^{152m}Eu	SIRIC	2.903(46)	1.1673	−59.80
^{152}Eu	NPL	11.190(75)	–	–
^{153}Gd	SIRIC	1.222(32)	1.2525	2.53

The sources of uncertainty of the half-life were evaluated in accordance with the proposed methodology by Pommé (2015), whereby the relative uncertainty of the activity for the component, $\sigma(A)/A$, are defined by their frequency in the measured dataset (i.e. low-, medium-, and high-frequency). The uncertainty components are estimated for the high- and medium-frequency components using the formula (Pommé and De Hauwere, 2020):

$$\frac{\sigma(T_{1/2})}{T_{1/2}} = \frac{2}{\lambda T}\sqrt{\frac{3(n-1)}{n(n+1)}}\ \frac{\sigma(A)}{A} \tag{3}$$

whilst the low-frequency components are estimated using the formula (Pommé and De Hauwere, 2020):

$$\frac{\sigma(T_{1/2})}{T_{1/2}} \approx \frac{2}{\lambda T}\left\langle\frac{\sigma(A)}{A}\right\rangle \tag{4}$$

where λ is the decay constant, T is the duration of the measurement campaign and n is the number of measurement data points. This propagation formula is robust where the occurrences of the uncertainty component are performed equidistant in time over the measurement campaign. In practice, this method also provides a relatively robust approximation where data sets loosely comply with this condition (Pommé and De Hauwere, 2020).

The high-frequency and medium-frequency components within the residuals of the WLS fit have been investigated using an empirical mode decomposition algorithm (Pommé and Pelczar, 2021). Through this

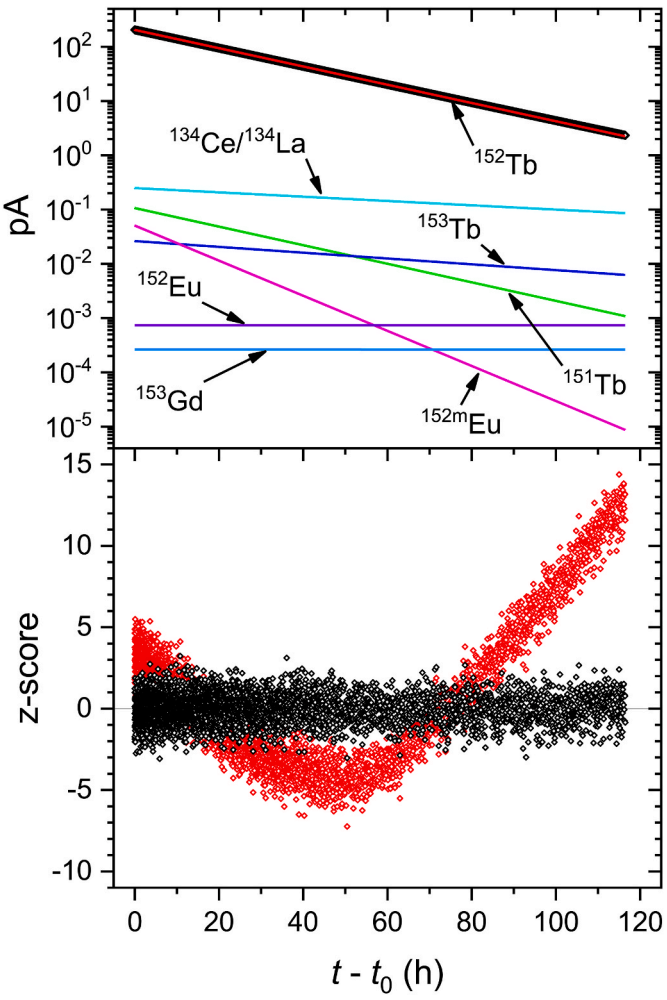

Fig. 4. The weighted non-linear least squares fit to the observed pA (top) and residuals (as z-score) for the VINTEN 671 ionisation chamber dataset. The red diamond residuals indicate the WLS fit to the dataset when no contaminants are included, whilst the black diamond residuals represent the WLS fit including all contaminants. (For interpretation of the references to colour in this figure legend, the reader is referred to the web version of this article.)

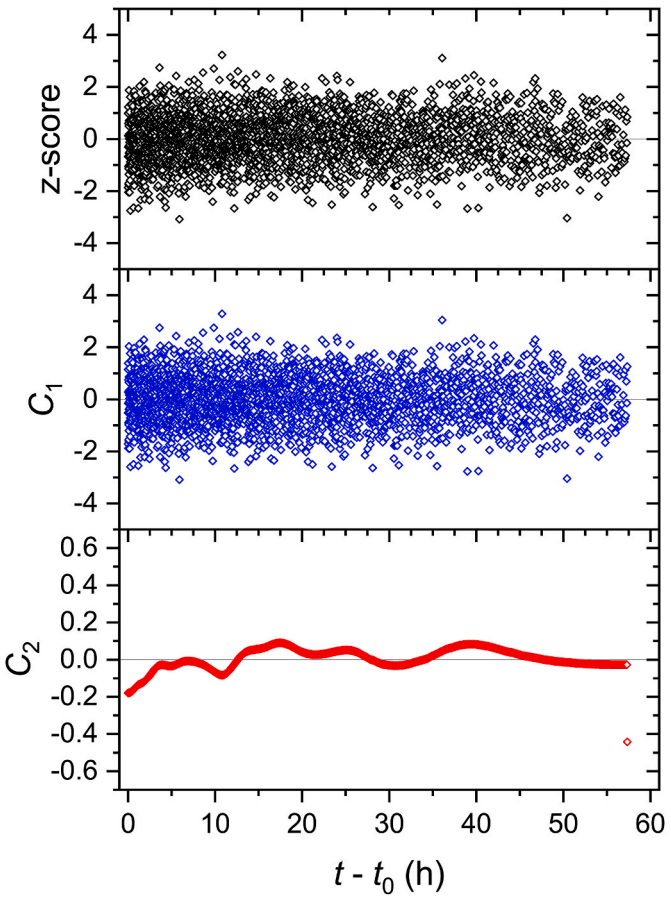

Fig. 5. Empirical mode decomposition of the residuals to the weighted least-squares fit of the observed data collected with the VINTEN 671 ionisation chamber. The random statistical component (C_1) and the medium-frequency component (C_2) are shown.

observable and obfuscated structures have been extracted from the residuals of the WLS fit. The decomposed statistical (C_1) and medium-frequency (C_2) modes from the residuals are shown in Fig. 5. The hypothetical bias to the half-life calculated as a function of time for each mode, and an envelope uncertainty function covering the absolute values of the biases over the measurement campaign are shown in Fig. 6.

The low-frequency components were identified as the linearity of the chamber and digital voltmeter (DVM), stability of the chamber, background, and contaminant correction. The stability uncertainty of 0.02 % has been estimated from daily quality check measurements using ^{226}Ra and ^{241}Am that have been performed on the IC for many years. The estimate of the stability uncertainty has been taken from linearity checks previously performed using ^{18}F over the range 550 pA–1 pA, which covers the range in this measurement campaign. This provides an uncertainty value of 0.10 % for the linearity. A 5 % uncertainty has been assigned to the background value and propagated for each measurement, thus the average of this propagated uncertainty to the first and final measurement used is taken as the estimate of the background uncertainty value. For each of the contaminants, the relative difference of the modelled and the WLS fit calibration factors was used as a basis for the uncertainty for the initial I of each contaminant. The activity uncertainty determined by HPGe gamma-ray spectrometry was combined in quadrature with the relative difference for each radionuclide contaminant. This uncertainty was propagated for the correction of each data point and the average of the first and last data point used as the estimate for the contaminant correction for each radionuclide. Using Eq. (4), these estimates of the uncertainty components were propagated as a function of time to provide an evolution of the half-life uncertainty. As shown in Fig. 7, whilst initially the precision of the half-life increases, after approximately 59.7 h no further improvement to the precision was achieved due to the influence of the ^{134}Ce contaminant correction. The half-life was therefore determined using 3479 data points collected over 59.76 h from the total 4437 data points. The half-life of ^{152}Tb determined via the VINTEN 671 IC was 17.893(28) h, the uncertainty budget is shown in Table 6.

2.4.2. *HPGe gamma-ray spectrometry – sample 1*

The HPGe gamma-ray spectrometer 'THOR' (as described in section 2.3.2) was used to follow the radioactive decay rate of the characteristic 271.1 keV, 344.3 keV, 586.3 keV gamma rays and the 511 keV gamma rays from the positron annihilation. The spectra were collected using a LYNX digital signal analyser (DSA) operating in loss-free counting (LFC) mode to provide the correction for the dead time and pulse pile-up. The measurement campaign began on 28 June 2018 for approximately 121 h (approximately 6.8 half-lives of ^{152}Tb). The measurement duration started at 1800 s, which increased to 2700 s and 5400 s at $t = 20$ h and $t = 59$ h, respectively. A total of 126 spectra were collected.

The regions of interest for the gamma-ray emissions were selected, and the peak areas determined using an internally developed Microsoft Excel based software package (Collins et al., 2020). For each gamma ray, the net peak area was determined from the sum of the channels after

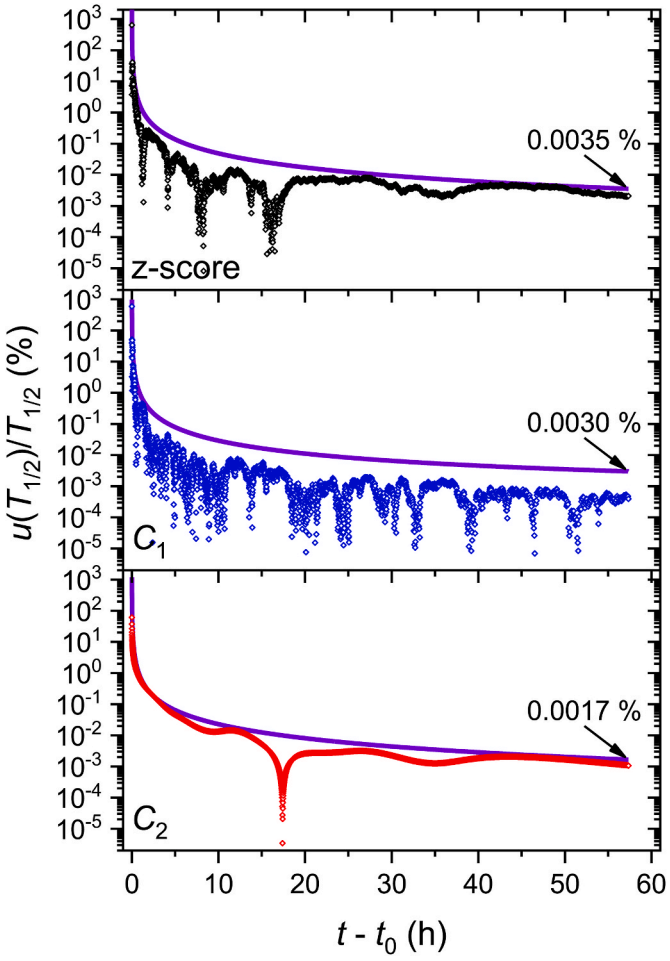

Fig. 6. The relative uncertainty of the half-life for the decomposition mode C_1 and C_2 as a function of time for the VINTEN 671 ionisation chamber residuals. The purple line represents their envelope function, with their ultimate uncertainty values indicated. (For interpretation of the references to colour in this figure legend, the reader is referred to the web version of this article.)

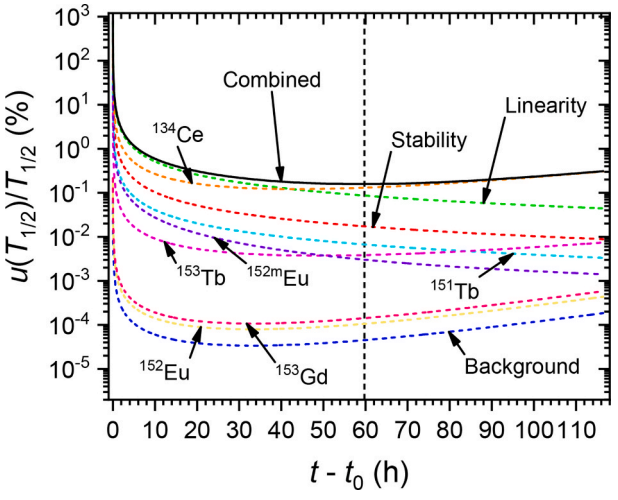

Fig. 7. Evolution of the propagated low-frequency uncertainty components of the half-life with time for the VINTEN 671 ionisation chamber. The optimum measurement duration for the uncertainty estimation is indicated by the vertical dashed line.

Table 6
Uncertainty budget for the half-life of ^{152}Tb determined by the VINTEN 671 ionisation chamber.

Component	$u(A)/A$ (%)	n	Propagation Factor	$u(T_{1/2})/T_{1/2}$ (%)
Statistical (C_1)	–	–	–	0.0030
Medium-frequency (C_2)	–	–	–	0.0017
Linearity	0.10	1	0.8639	0.086
Stability	0.020	1	0.8639	0.017
Background	0.0052	1	0.8639	0.0045
Contaminant (^{151}Tb)	0.0078	1	0.8639	0.0067
Contaminant (^{153}Tb)	0.0045	1	0.8639	0.0039
Contaminant (^{134}Ce)	0.15	1	0.8639	0.13
Contaminant (^{152m}Eu)	0.0035	1	0.8639	0.0030
Contaminant (^{152}Eu)	0.00012	1	0.8639	0.00011
Contaminant (^{153}Gd)	0.00016	1	0.8639	0.00014
Combined standard uncertainty				0.16

continuum subtraction. The initial count rates were approximately 114 s^{-1}, 531 s^{-1}, 101 s^{-1} and 38 s^{-1} for the 271.1 keV, 344.3 keV, 511 keV and 586.3 keV gamma rays, respectively. No naturally occurring background, B, was observed for the characteristic gamma rays, whilst a background rate of 0.00739(37) s^{-1} was measured for the 511 keV FEP.

The gamma-ray emissions are shared by the detected contaminant ^{152m}Eu. The respective emission intensities (per 100 decays) of the 271.1 keV, 344.3 keV and 586.3 keV from the decay of this nuclei are 0.074(3), 2.38(3) and 0.0126(22) (Martin, 2013). However, for the same gamma-ray emissions from the decay of ^{152}Tb the intensities are 9.53(21), 63.5(17) and 9.21(21), respectively. Considering the activity ratio at the start of the measurement campaign (see Fig. 2) and the ratio of the gamma-ray emission intensities of the ^{152m}Eu to ^{152}Tb along with the ratio of the respective half-lives then we can consider that the impact on the half-life determinations should be negligible (the FEP detection efficiency can be ignored as these will be identical for each respective energy). The impact of ^{152}Eu can also be ignored. However, for the 511 keV the positron decays from the ^{134}Ce–^{134}La do have to be accounted for; however, due to the different positron energies the detection efficiencies will vary (the ^{151}Tb and ^{153}Tb can be ignored due to their very small positron branch ratios). In this work, no account has been made to determine the difference in the detection efficiency for the 511 keV gamma rays.

The datasets for each gamma-ray emission were fitted using a non-linear least squares fit using the expression:

$$R_t = R_0 e^{-\lambda_{Tb-152} t} \frac{1 - e^{-\lambda_{Tb-152}\Delta t}}{\lambda_{Tb-152}\Delta t} \tag{5}$$

where R_t and R_0 are the count rates at time t and t = 0, respectively.

The dataset for the 511 keV was fitted with:

$$R_t = R_0 e^{-\lambda_{Tb-152} t} \frac{1 - e^{-\lambda_{Tb-152}\Delta t}}{\lambda_{Tb-152}\Delta t} + R_0 e^{-\lambda_{Ce-134} t} \frac{1 - e^{-\lambda_{Ce-134}\Delta t}}{\lambda_{Ce-134}\Delta t} + B \tag{6}$$

The weight for each datum was composed of the net peak area uncertainty (composed of the statistics and continuum subtraction components).

From the WLS fit, trends were observed in the residuals for each dataset, which indicated that there was a faster decay observed at the beginning of the campaign. The presence of ^{152m}Eu was considered and a least-squares fit was performed with an additional exponential term added to Eq. (5) where the activity of the ^{152m}Eu was set as a free parameter. Whilst this resolved the trends in the residuals the count rate required was significantly greater than what would be expected by several orders of magnitude. The half-life determined from a weighted mean of the three datasets using this method was 17.935 h. However, as discussed earlier when considering the activity determined and the gamma-ray emission intensities of ^{152}Tb and ^{152m}Eu this would appear to be unrealistic. Further investigation eventually led to the observation

that the resolution (FWHM) had undergone several significant step changes during the campaign. These changes in the FWHM for each FEP can be seen in Fig. 8.

The measurements occurred at a period when the UK was undergoing a significant heat wave which had resulted in the laboratory environmental controls being overwhelmed. The loss of environmental controls impacted some component in the electronics chain. It is considered that due to the changes in the width of these peaks this influenced the continuum subtraction (due to a change in the number of channels used) which led to a small change in the observed counts in the peak area. With the manner of half-life measurements, even small changes in the detector system can create significant changes in the observed decay rate that can be falsely attributed to other effects (Pommé et al., 2016).

As there is a period of stability in the FWHM from approximately 20 h–90 h (comprising of 67 data points) this was selected to determine the half-life. The WLS fit to the observed rates and the residuals (as the relative difference) for the fit to each gamma ray dataset are shown in Fig. 8, this includes the rejected data showing the deviation from the selected data.

The uncertainty components were treated in the same manner as for the ionisation chamber (see section 2.4.1). The high- and medium-frequency components within the residuals of the WLS fit have been investigated using an empirical mode decomposition algorithm (Pommé and Pelczar, 2021). This resulted in a decomposed statistical (C_1), a medium-frequency (C_2), and a second slower medium-frequency (C_3) modes from the residuals (Fig. 9). The hypothetical bias to the half-life calculated as a function of time for each mode, and an envelope uncertainty function covering the absolute values of the biases over the measurement campaign are shown in Fig. 10.

The low-frequency components were identified as the dead time and pulse pile-up (i.e. linearity), detection efficiency stability across all the gamma ray datasets used, with the addition of components for the naturally occurring background correction and presence of the ^{134}Ce contaminant for the 511 keV FEP. The background and ^{134}Ce count rate were attributed uncertainties of 5% and 20%, respectively, these were propagated to each measurement. The $u(A)/A$ value for the background and contaminant has been estimated by taking the average of the propagated uncertainty on the initial and final measurements. This average value was propagated using Eq. (4) to provide the $u(T_{1/2})/T_{1/2}$ value. The linearity of the DSA operating in LFC mode has previously been validated at NPL up to a dead time of 10 % using a ^{57}Co and ^{60}Co source fixed in position and varying the count rate imposed on the detector using either a ^{133}Ba or ^{131}I source. By comparison of count rates of the 122.1 keV and 1332.5 keV FEPs of ^{57}Co and ^{60}Co, respectively, at different dead times the DSA was estimated to correct for the dead time and pulse-pile-up to within 0.10 %. The detection efficiency stability of the 'THOR' has been monitored at weekly intervals over its operational lifetime using a ^{152}Eu source. The uncertainty for the detection efficiency stability from these measurements has been estimated at 0.10 %. These linearity and stability components were correlated across both gamma-ray emissions and thus combined in quadrature into the final uncertainty.

The half-life determined for each gamma ray dataset and the standard uncertainty determined from the C_1, C_2, C_3, contaminant, and background uncertainty components are provided in Table 7. The final half-life was determined from the weighted mean of the four datasets, using their combined uncertainty to provide the weight factor (Table 7), with the standard uncertainty derived from combining the uncertainty of the weighted mean with the correlated low-frequency components in quadrature. The half-life determined by HPGe gamma-ray spectrometry for Sample 1 was 17.861(21) h.

2.4.3. *HPGe gamma-ray spectrometry – sample 2*

The HPGe gamma-ray spectrometer 'LOKI' (as described in section 2.3.2) was used to measure the radioactive decay rate of ^{152}Tb utilising the gamma rays as identified in section 2.4.2. The spectra were collected

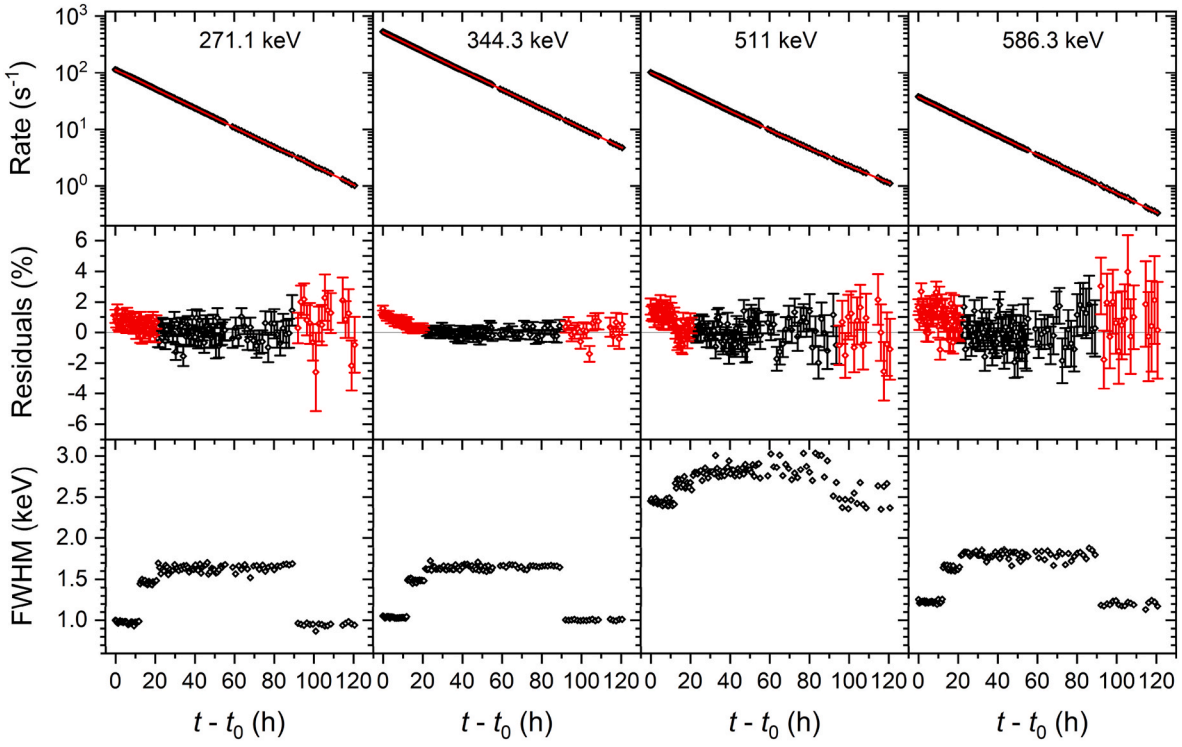

Fig. 8. The weighted least-squares fit to the observed rates (top), the relative residuals of the fits (middle) and resolution (FWHM) over the campaign period (bottom) for the 271.1 keV, 344.3 keV, 511 keV and 586.3 keV datasets. The red data points in the middle figure indicate those datum that were rejected from the analysis due to the instability of the resolution (FWHM). (For interpretation of the references to colour in this figure legend, the reader is referred to the web version of this article.)

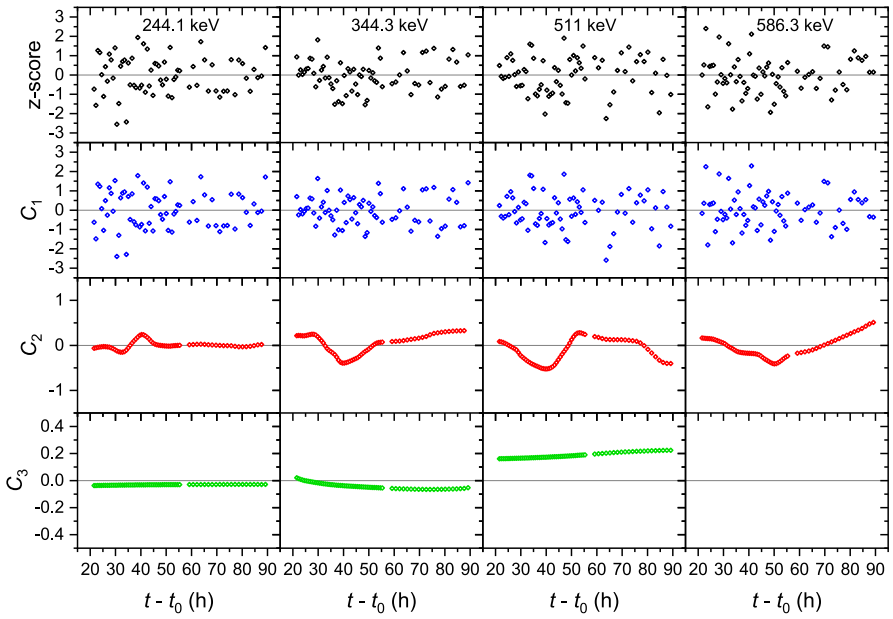

Fig. 9. Empirical mode decomposition of the residuals to the weighted least-squares fit of the 244.1 keV, 344.3 keV, 511 keV and 586.3 keV data sets measured by the HPGe gamma-ray spectrometer 'THOR'. The random statistical component (C_1), a medium-frequency component (C_2), and a slower medium-frequency component (C_3) are shown (no C_3 component was identified for the 586.3 keV).

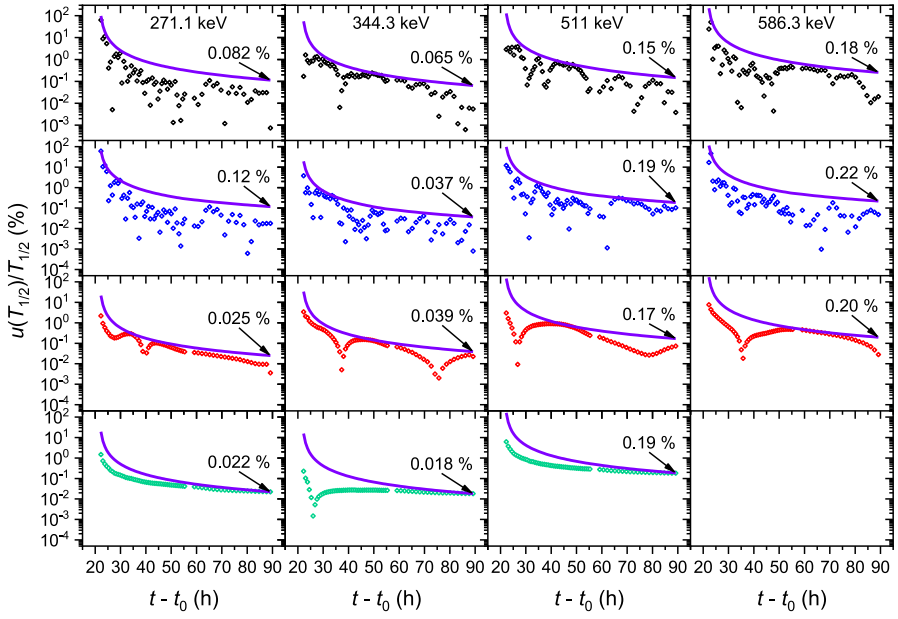

Fig. 10. The relative uncertainty of the half-life for the decomposition modes C_1, C_2 and C_3 as a function of time for the 271.1 keV, 344.3 keV, 511 keV and 586.3 keV residuals. The purple line represents their envelope function, with their ultimate uncertainty values indicated. (For interpretation of the references to colour in this figure legend, the reader is referred to the web version of this article.)

using a LYNX digital signal analyser (DSA) operating in loss-free counting (LFC) mode to provide the correction for the dead time and pulse pile-up. The measurement campaign began on 1 April 2022 for approximately 128.5 h (approximately 7.2 half-lives). The measurement time started at a pre-set live time of 600 s, which increased to 900 s, 1200 s and 1800 s at $t = 18.0$ h, t = 44.6 h, and $t = 78.4$ h, respectively. However, the real time of each measurement was longer dependent on the dead time during the measurement. A total of 401 spectra were collected.

The net peak area for each FEP was determined in the same manner as in section 2.4.2. The initial count rates were approximately 75 s^{-1}, 374 s^{-1}, 78 s^{-1} and 30 s^{-1} for the 271.1 keV, 344.3 keV, 511 keV and 586.3 keV gamma rays, respectively. No naturally occurring background, B, was observed for the gamma rays, a background rate of 0.00462(23) s^{-1} was measured for the 511 keV FEP. As a result of the previous issues of the resolution in 2018, the stability of the resolution was reviewed with no instability found during this measurement campaign.

Table 7
The half-life and uncertainty budget for the HPGe gamma-ray spectrometry measurement of Sample 1.

Component	271.1 keV	344.3 keV	511 keV	586.3 keV
	$\sigma(T_{1/2})/T_{1/2}$ (%)	$\sigma(T_{1/2})/T_{1/2}$ (%)	$\sigma(T_{1/2})/T_{1/2}$ (%)	$\sigma(T_{1/2})/T_{1/2}$ (%)
C_1	0.12	0.037	0.19	0.22
C_2	0.025	0.039	0.17	0.20
C_3	0.022	0.018	0.19	–
Contaminant	–	–	0.86	–
Background	–	–	0.0046	–
$T_{1/2}$/gamma ray	17.849(31) h (± 0.17 %)	17.864(10) h (± 0.058 %)	17.76(17) h (± 0.94 %)	17.855(63) h (± 0.35 %)
	$\sigma(A)/A$(%)	***n***	**Propagation factor**	**$\sigma(T_{1/2})/T_{1/2}$(%)**
Weighted mean	–	–	–	0.051
Linearity	0.10	1	0.762	0.076
Stability	0.10	1	0.762	0.076
$T_{1/2}$	17.861(21) h			0.12

As there were no identified interfering impurities for the gamma rays, the datasets for the 271.1 keV, 344.3 keV and 586.3 keV gamma rays were fitted using Eq. (5), using the same procedure to define the weight for each datum. Due to the presence of ^{153}Tb, which became more significant as the ^{152}Tb decayed (see Fig. 3), Eq. (6) was used with the $\lambda_{\text{Ce-134}}$ replaced with $\lambda_{\text{Tb-153}}$. The WLS fit to the observed count rate and residuals of the fit are shown in Fig. 11.

The uncertainty components were reviewed in an identical manner to that described in section 2.4.2. The empirical decomposition modes are shown in Fig. 12. The hypothetical bias to the half-life calculated as a function of time for each mode, and an envelope uncertainty function covering the absolute values of the biases over the measurement campaign are shown for each gamma ray dataset in Fig. 13. The low-frequency components are the same as described for the HPGe gamma-ray spectrometer 'THOR'.

As with the Sample 1 by 'THOR', the half-life was determined from the weighted mean of the four gamma-ray datasets, with the correlated uncertainty components combined in quadrature with the standard uncertainty of the weighted mean. The half-life determined for each gamma ray and the uncertainty budget are presented in Table 8. The half-life determined by the HPGe gamma-ray spectrometer 'LOKI' for Sample 2 was 17.882(12) h.

2.4.4. Liquid scintillation counting – sample 2

The liquid scintillation counting was performed using a Hidex 300SL counter, which is an automatic system that incorporates three photomultiplier tubes (PMTs) that allow for the use of the triple-to-double coincidence (TDCR) counting technique. This system has previously been used successfully for the half-life determination of ^{155}Tb at NPL (Collins et al., 2022b). A background vial, of matching geometry and chemistry, and the two active vials prepared in section 2.3.1 (henceforth known as vial A and vial B), were placed sequentially in the counter. The counter was set to cycle through single measurements of the background and the two active samples in order. The measurement campaign commenced on 31 March 2022 and continued for 530 h, collecting 288 measurements for each of the background and two active samples. The logical sum of doubles (LSD) counts, R_D, and triple counts, R_T, were collected for each measurement. The measurement time for each measurement was initially 600 s, increasing to 900 s, 1800 s and 3600 s at t = 74.8 h, t = 119.5 h, and t = 194.9 h, respectively.

As has been discussed in (Kossert et al., 2020), the TDCR offers benefits in certain situations where a temporally stable counting efficiency can provide an indication of the temporally stable TDCR parameter (TDCR = R_T/R_D). Unfortunately, in this work, due to the presence of significant contaminants in Sample 2 (see Table 4 and Fig. 3) the TDCR parameter changed over the measurement campaign (Fig. 14). This is due to the activity of the ^{153,155}Tb contaminants and the ^{151} Gd decay progeny increasing as a ratio of the total activity over the campaign (Fig. 3). These have a higher proportion of internal conversion than ^{152}Tb that result in a higher detection efficiency as a function of the TDCR parameter.

The R_D and R_T for each datum was determined using

$$R_x = \frac{N_x - B_x}{\Delta t} k_t \tag{7}$$

where R_x is the rate of the LSD or triples, N_x is the total counts of the LSD or triples collected in the counting period Δt, B_x is the background counts of the LSD or triples measured at the beginning of the cycle, and k_t is the correction factor for the dead time.

A WLS fit was performed to the LSD and triples count rates of the vial A and vial B datasets using:

$$R(t) = \sum \left(R_n \bullet e^{-\lambda_n t} \bullet \frac{1 - e^{-\lambda_n \Delta t}}{\lambda_n \Delta t} \right) \tag{8}$$

where R_n and λ_n are the contribution and decay constant of each radionuclide present, respectively, which had been identified as ^{151}Tb, ^{152}Tb, ^{153}Tb, ^{155}Tb, ^{151}Gd, ^{153}Gd and ^{139}Ce. For the WLS, the

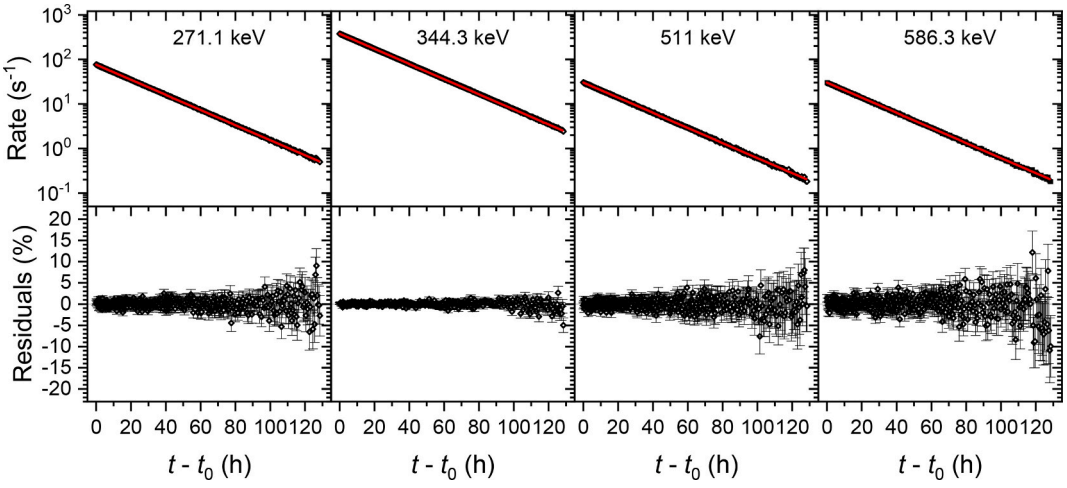

Fig. 11. The weighted least-squares fit to the observed rates (top) and the relative residuals of the fits (bottom) for the 271.1 keV, 344.3 keV, 511 keV and 586.3 keV datasets from Sample 2.

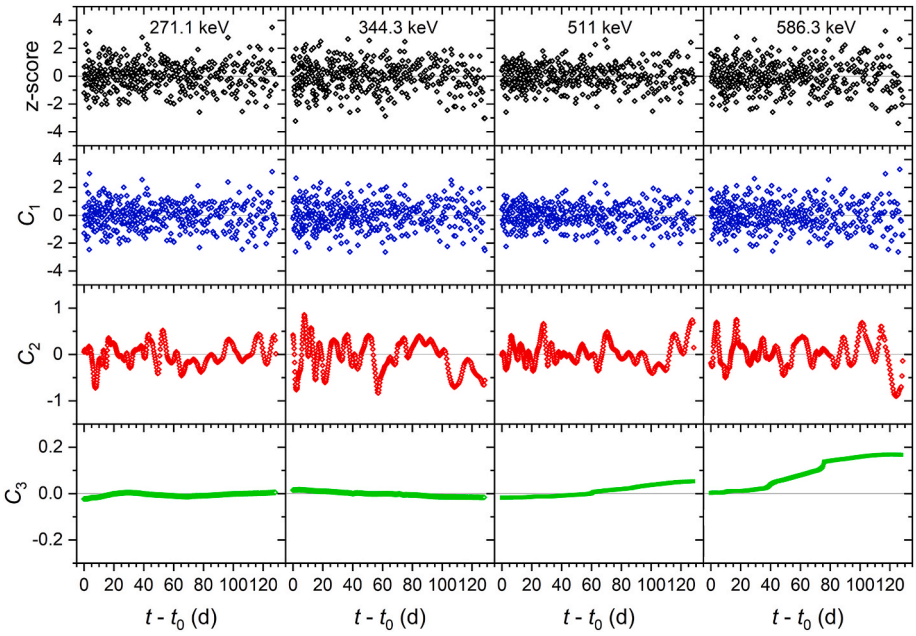

Fig. 12. Empirical mode decomposition of the residuals to the weighted least-squares fit of the 244.1 keV, 344.3 keV, 511 keV and 586.3 keV data sets measured by the HPGe gamma-ray spectrometer 'LOKI' for Sample 2. The random statistical component (C_1), a medium-frequency component (C_2), and a slower medium-frequency component (C_3) are shown.

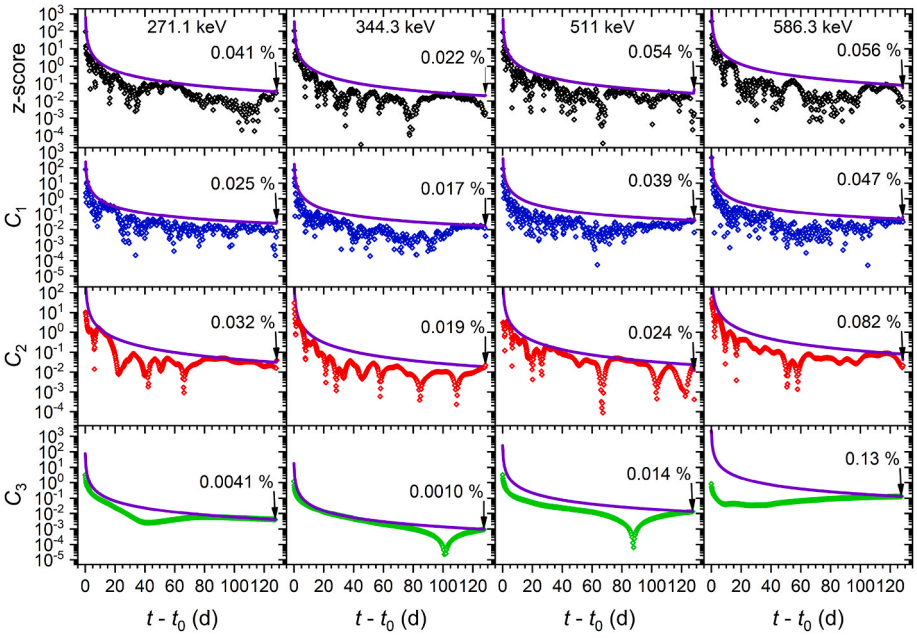

Fig. 13. The relative uncertainty of the half-life for the decomposition modes C_1, C_2 and C_3 as a function of time for the 271.1 keV, 344.3 keV, 511 keV and 586.3 keV residuals. The purple line represents their envelope function, with their ultimate uncertainty values indicated. (For interpretation of the references to colour in this figure legend, the reader is referred to the web version of this article.)

contribution for each radionuclide and decay constant of ^{152}Tb were free parameters with the decay constant of all contaminants fixed. As an initial starting condition, the count rates were set as per the activity ratios at the start of the measurement campaign. The WLS fit of the ^{152}Tb and contaminants to the observed count rate for the LSD of vial A and the relative residuals are shown in Fig. 15. It should be noted that no attempt has been made to model the detection efficiencies for each of the radionuclides. As a result, the uncertainties of each of the contaminants have been inflated.

However, as with the ionisation chamber determination, it is not always favourable to use the complete dataset as the uncertainties of the low-frequency components can result in the combined standard uncertainty of the half-life increasing. Analysis of the evolution of the uncertainty propagation of the low-frequency components shows that the combined standard uncertainty begins to increase after 60 h, due to the presence of the long-lived contaminants (Fig. 16). Therefore, the WLS was repeated using a reduced dataset of 104 data points. The $R_{\text{Gd-151}}$, $R_{\text{Gd-153}}$, $R_{\text{Tb-155}}$, and $R_{\text{Ce-139}}$ parameters were fixed in this instance as the reduced dataset did not provide the least-squares fit process sufficient data to fit this in a realistic manner. The half-life determined for the LSD

Table 8
The half-life and uncertainty budget for the HPGe gamma-ray spectrometry measurement of Sample 2.

Component	271.1 keV	344.3 keV	511 keV	586.3 keV
	$\sigma(T_{1/2})/T_{1/2}$ (%)	$\sigma(T_{1/2})/T_{1/2}$ (%)	$\sigma(T_{1/2})/T_{1/2}$ (%)	$\sigma(T_{1/2})/T_{1/2}$ (%)
C_1	0.025	0.017	0.039	0.047
C_2	0.032	0.019	0.024	0.082
C_3	0.0041	0.0010	0.014	0.13
Contaminant			0.23	
Background			0.0084	
$T_{1/2}$ / **gamma ray**	17.8965(72) h (± 0.040 %)	17.8760(46) h (± 0.026 %)	17.872(43) h (± 0.24 %)	17.896 (29) h (± 0.16 %)
	σ(A)/A(%)	**N**	**Propagation factor**	**σ($T_{1/2}$)/$T_{1/2}$(%)**
Weighted mean	–	–	–	0.030
Linearity	0.10	1	0.401	0.040
Stability	0.10	1	0.401	0.040
$T_{1/2}$	17.882(12) h			0.064

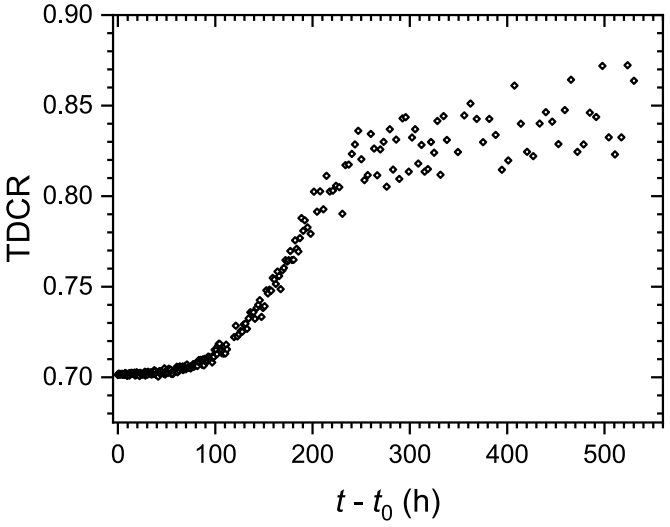

Fig. 14. The observed TDCR parameter throughout the measurement campaign for vial A. The trend of the TDCR parameter observed presented is representative of the trend for both vials.

and triples for vial A and B are given in Table 9. The half-lives determined for each dataset showed a significant spread (standard deviation = 0.10 %) in the results with respect to their uncertainties derived from their high-frequency and medium-frequency components. This was considered a result of the complexity of accurately fitting six contaminants with different detection efficiencies. However, as can be seen in Table 9 the spread in results is adequately covered by the final combined uncertainty when the low-frequency components are considered.

The uncertainty components have been considered in the same manner as for the other techniques. The empirical decomposition modes are shown in Fig. 17. The hypothetical bias to the half-life calculated as a function of time for each mode, and an envelope uncertainty function covering the absolute values of the biases over the measurement campaign are shown for each gamma-ray dataset in Fig. 18.

The low-frequency components have been identified as the linearity of the detector response, stability of the detector system and scintillation cocktail, background, and contaminants. The linearity has previously been determined using a ^{18}F source, with an estimate of 0.10% for the uncertainty of this component. Due to the presence of the contaminants,

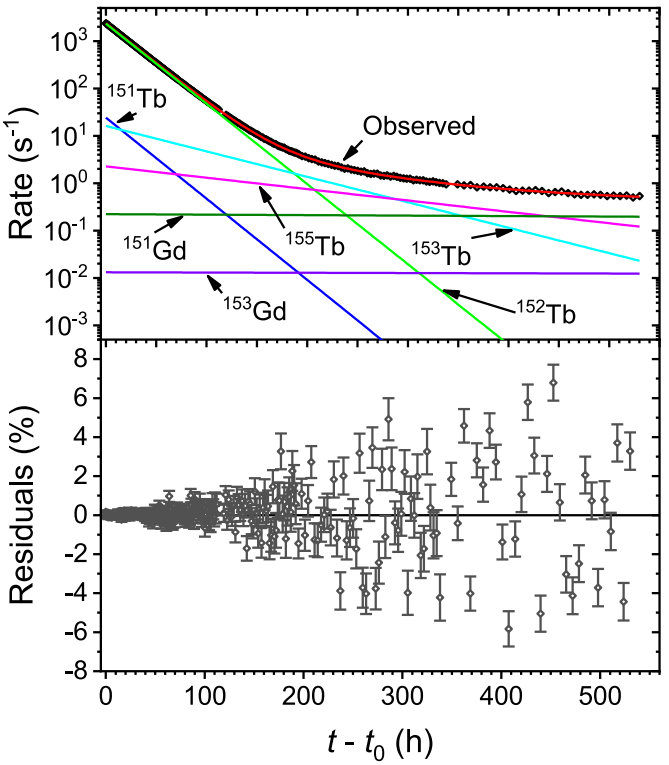

Fig. 15. The weighted least-square fit of ^{152}Tb and the contaminants to the observed rate (top) and the relative residuals of the fit (bottom) to the LSD dataset for vial A.

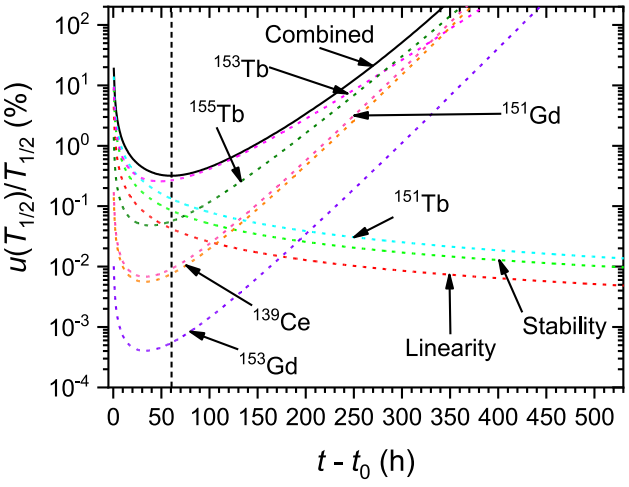

Fig. 16. Evolution of the propagated low-frequency uncertainty components of the half-life with time for the liquid scintillation counting using the TDCR technique. The optimum measurement duration for the uncertainty estimation is indicated by the vertical dashed line.

the temporal stability cannot be assessed by the analysis of the TDCR parameter (Fig. 14). We have therefore chosen to take the estimate of the stability from a previous study of ^{155}Tb which utilised the same detector, chemistry, and liquid scintillation cocktail (Collins et al., 2022b). As shown in Fig. 16, the contaminants are a dominant factor in the uncertainty of the half-life estimate. The uncertainty for the R for the contaminants has been estimated from the relative difference of the activity ratio determined in Table 4 and the activity ratio determined by the WLS fit for the datasets. This was then propagated for each datum of

Table 9
The half-life and uncertainty budget for the liquid scintillation counting measurement of Sample 2. The half-lives determined for each of the Vial A and B LSD and triples datasets are given.

Component	Vial A		Vial B	
	LSD	Triples	LSD	Triples
	$\sigma(T_{1/2})/T_{1/2}$ (%)	$\sigma(T_{1/2})/T_{1/2}$ (%)	$\sigma(T_{1/2})/T_{1/2}$ (%)	$\sigma(T_{1/2})/T_{1/2}$ (%)
C_1	0.015	0.025	0.019	0.023
C_2	0.024	0.025	0.039	0.049
C_3	0.0081	0.016	0.0072	0.0023
$T_{1/2}$	17.8151 (81) h (± 0.029 %)	17.8374 (69) h (± 0.039 %)	17.7941(80) h (± 0.045 %)	17.8274 (97) h (± 0.054 %)
	$\sigma(A)/A$ (%)	***n***	**Propagation factor**	**$\sigma(T_{1/2})/T_{1/2}$ (%)**
Weighted mean	–	–	–	0.048
Linearity	0.10	1	0.8482	0.085
Stability	0.10	1	0.8482	0.085
Background	0.012	1	0.8482	0.010
Contaminant (^{151}Tb)	0.30	1	0.8482	0.25
Contaminant (^{153}Tb)	0.51	1	0.8482	0.43
Contaminant (^{155}Tb)	0.12	1	0.8482	0.10
Contaminant (^{139}Ce)	0.010	1	0.8482	0.0087
Contaminant (^{151}Gd)	0.012	1	0.8482	0.010
Contaminant (^{153}Gd)	0.00085	1	0.8482	0.00072
$T_{1/2}$	17.818(94) h			0.53

the datasets to provide an uncertainty for the contaminant correction. The average of this propagated uncertainty of all the datasets for the first and final measurement used was applied to estimate the $u(A)/A$ value found in Table 9. The uncertainty on the background of 5% was estimated from the standard deviation of all background measurements, and the average of the propagated uncertainty for the first and final measurement used was taken as the $u(A)/A$ value. The full uncertainty budget is provided in Table 9.

In the same manner as for the half-life determinations by the HPGe gamma-ray spectrometry technique, a weighted mean of the four half-lives was calculated using the C_1, C_2, and C_3 uncertainties combined in quadrature as the weight factor. The final uncertainty of the half-life was then determined by combining the standard uncertainty of the weighted mean with the low-frequency uncertainty components. The half-life determined by liquid scintillation counting using the TDCR technique was 17.818(94) h.

3. Discussion

3.1. Half-life

In Table 10 a summary of the four half-life determinations of ^{152}Tb made by the three independent techniques of ionisation chamber measurement, HPGe gamma-ray spectrometry, and liquid scintillation counting from two separate productions is provided. The four determinations agree where $\chi^2/\nu = 0.50$. As a result of contaminants in the samples the HPGe gamma-ray spectrometry technique was ultimately the most precise of the three techniques since it had no sensitivity to the contaminants present. The magnitude of the contaminants has restricted the precision achievable by the IC and LS techniques, severely in the case of the LS technique. The WLS fit analysis for the IC and LS techniques also relies on the accuracy of the half-lives used. Whilst the half-life of ^{155}Tb has recently been measured in Collins et al. (2022b) the half-lives of the significant contaminants are based upon a single determination or small literature datasets from the 1980s or earlier (Nica, 2020; Singh, 2009; Sonzogni, 2004). Significant changes to these half-lives in the future could alter the results of the half-lives determined for the IC and LS techniques. However, this will have a negligible impact on the half-life reported in this work as the statistical weight of the IC and LS techniques in the final averaged result are 0.1118 and 0.0101, respectively. The agreement between all four determinations when considering the different sensitivities of the techniques and the difference in

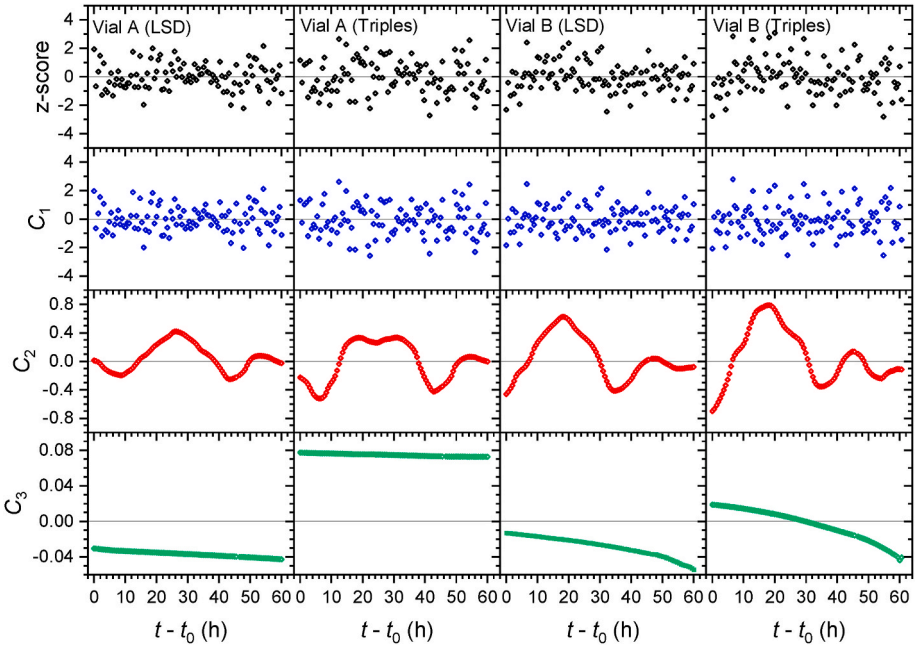

Fig. 17. Empirical mode decomposition of the residuals to the weighted least-squares fit of the LSD and triples datasets for Vial A and B measured by Liquid scintillation counting for Sample 2. The random statistical component (C_1), a medium-frequency component (C_2), and a slower medium-frequency component (C_3) are shown.

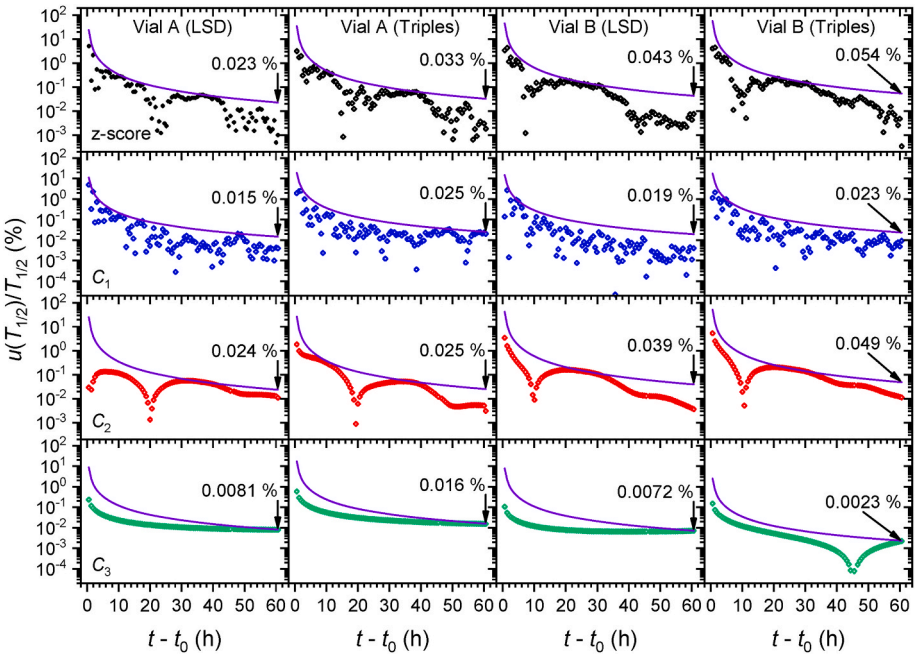

Fig. 18. The relative uncertainty of the half-life for the decomposition modes C_1, C_2 and C_3 as a function of time for the Vial A and B LSD and triples dataset residuals. The purple line represents their envelope function, with their ultimate uncertainty values indicated. (For interpretation of the references to colour in this figure legend, the reader is referred to the web version of this article.)

Table 10
Summary of half-life measurements made by the different techniques for the two samples.

Technique	Sample	Total measurement time(h)	Measurement time used(h)	Number of $T_{1/2}$'s	Statistical Weight	$T_{1/2}$ (h)	$u(T_{1/2})/T_{1/2}$ (%)
Ionisation chamber	1	116.5	59.8	3.34	0.1118	17.893(28)	0.16
HPGe	1	120.7	67.6	3.79	0.2026	17.861(21)	0.12
HPGe	2	128.5	128.5	7.18	0.6754	17.882(12)	0.079
LS	2	530.2	60.6	3.40	0.0101	17.818(94)	0.53
Weighted mean						17.8784(95)	0.053
χ^2/ν						0.50	

the samples provides confidence in the accuracy of the half-life determinations and the standard uncertainties attributed to each. A weighted mean of these four determinations gives $T_{1/2}(^{152}\text{Tb}) = 17.8784(95)$ h.

This half-life shows a significant difference (ζ-score = 3.77) to the currently evaluated half-life in (Martin, 2013), with a relative difference of 2.2 %. The half-life determined here also provides an order of magnitude improvement on the precision of the half-life. The half-life value evaluated by (Martin, 2013) stems from the only two previous half-life determinations made by Gromov et al. (1967), utilising a six-gap β-spectrometer, and Toth et al. (1960), from a weighted mean of measurements made of two samples by a gas-flow proportional counter and a scintillation gamma-spectrometer. Though, when referring to the evaluation rules of the Decay Data Evaluation Project (Bé et al., 1999), these two previous determinations include the same contributing authors and may be considered as one set of work using three techniques. The comparison of the determinations made in this work and those determinations is shown in Fig. 19. Both Toth et al. (1960) and Gromov et al. (1967) used mass separated samples, however, unlike in this work they have not provided any analysis of the contaminants in the samples that they have used nor provide details of how they have accounted for these in their determinations. As shown in the current work, it is vital to account for the contaminants to determine an accurate half-life. It is worth noting that in Collins et al. (2022b), the half-life of ^{155}Tb determined in that study also showed a 3% relative deviation to the value determined in Toth et al. (1960).

The standard uncertainty of the half-life quoted in this work is an order of magnitude more precise than previously quoted. The impact of this improvement in precision is demonstrated in Fig. 20, where the contribution of the standard uncertainty of the half-life propagated to the uncertainty of the activity is reduced from 2.0 % to 0.21 % at $(t - t_0) = 90$ h (approximately five half-lives).

3.2. Purity of ^{152}Tb samples

The presence of radionuclide contaminants effects on this half-life determination have been discussed and identified as problematic for certain techniques. However, for the intended use of ^{152}Tb as a radiopharmaceutical for diagnostic applications the purity level of the produced samples is of utmost importance to ensure patient safety and manage waste clearance, with the level of radionuclide purity fulfilled throughout the shelf-life of the radiopharmaceutical. Therefore, it is important to identify if mass separation to purify samples is sufficient, if an additional radiochemical purification step is required, and if its addition will provide the purity required. In Tables 2 and 4, the summary of the contaminants identified for sample 1 (without radiochemical separation) and 2 (with radiochemical separation) is presented, both showing the presence of ^{151}Tb and ^{153}Tb due to high- and low-energy mass tailing from the mass separation process. At the EoC for sample 1 the ^{151}Tb and ^{153}Tb are 0.050 % and 0.010 %, respectively, however, for sample 2 these have increased to 0.99 % and 0.092 %. The differences in these ratios are due to the conditions of the mass-separation process (ion source settings, beam tuning, slit positions, and beam line collection) but it shows that under the correct conditions the high- and

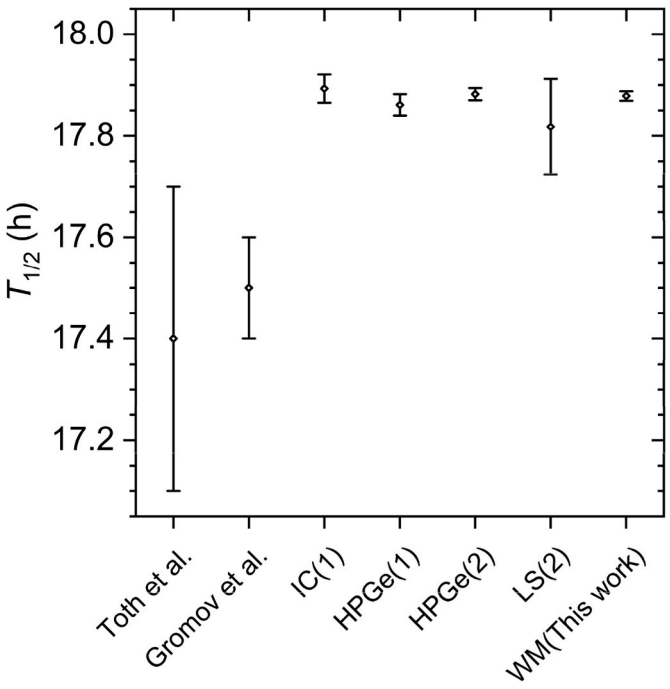

Fig. 19. The half-life determinations for ^{152}Tb from the literature and this work. The number in brackets after the technique identifies the sample. The measurement techniques utilised by Toth et al. (1960) and Gromov et al. (1967) are identified in the main text of section 3.1.

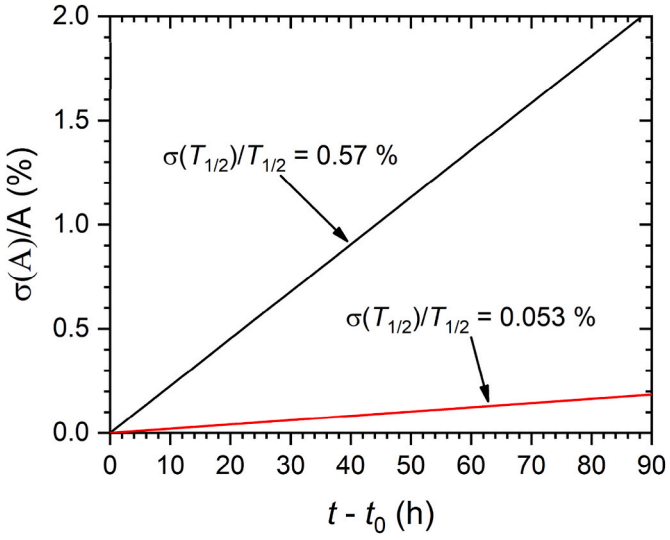

Fig. 20. The uncertainty propagation of the standard uncertainty of the half-life for ^{152}Tb to the uncertainty of the activity (arbitrarily over approximately five half-lives) for the evaluated half-life (black line) and quoted in this work (red line). (For interpretation of the references to colour in this figure legend, the reader is referred to the web version of this article.)

low-mass separation tailing can be controlled sufficiently to produce samples of high purity of the two terbium radioisotopes. As shown in Fig. 2, due to the similar half-life of the ^{151}Tb and ^{152}Tb the activity ratio will not change significantly, whilst the ^{153}Tb takes almost five half-lives of ^{152}Tb to become more than 0.1 % of the activity of the solution. This would bode well for the 'shelf-life' of any radiopharmaceutical. The collection of ^{152m}Eu and ^{134}Ce, as the pseudo-isobaric ^{134}Ce^{18}O, results in significant quantities of ^{152m}Eu collected and small quantities of ^{134}Ce but, as shown in Fig. 2, their respective activity ratio results in the total contaminant ratio never dropping below 0.3 %. The addition of a radiochemical purification stage is therefore important to provide a high purity sample of ^{152}Tb. For sample 2, the addition of a radiochemical purification stage appears to result in the removal of ^{134}Ce, with none detected in the HPGe gamma-ray spectrometry measurements, though the detection limit is of a similar magnitude to the activity ratio identified in Sample 1 and therefore would require further investigation to confirm. With the capability to remove the ^{152m}Eu and ^{134}Ce contaminants via radiochemical purification (Webster et al., 2019) and where the ^{151}Tb and ^{153}Tb removal by mass separation is adequately controlled, high purity samples of ^{152}Tb can be produced suitable for radiopharmaceuticals.

4. Conclusion

There has been little investigation of the half-life of the diagnostic radioisotope ^{152}Tb, with only two determinations prior to the current work, and both with limited information on the systematic analysis of the uncertainties. As such, the current literature precision of the half-life is inconvenient for radioactive decay corrections even over short time frames. In the current work, the first half-life determination of ^{152}Tb since 1967 is presented. Two mass-separated samples, from CERN-ISOLDE in 2018 and 2022, have been used to make four half-life measurements by three independent techniques: ionisation chamber measurement, HPGe gamma-ray spectrometry, and liquid scintillation counting. The radionuclide contaminants have been assessed in each sample and accounted for in the analysis. For each determination the uncertainty budget has been assessed. Agreement was found between all four determinations and a new half-life of $T_{1/2}$(^{152}Tb) = 17.8784(95) h was determined from the weighted mean of these. This value has a relative difference of 2.2 % to the currently evaluated half-life and has an order of magnitude improvement to the precision. The performance of the mass-separation and the radiochemical separation of the radionuclide contaminants have been assessed and show that through the combination of these two techniques high purity samples can be produced.

CRediT authorship contribution statement

S.M. Collins: Writing – review & editing, Writing – original draft, Visualization, Validation, Supervision, Software, Resources, Project administration, Methodology, Investigation, Funding acquisition, Formal analysis, Data curation, Conceptualization. **U. Köster:** Writing – review & editing, Writing – original draft, Resources, Methodology, Investigation, Conceptualization. **A.P. Robinson:** Writing – review & editing, Resources, Conceptualization. **P. Ivanov:** Methodology, Investigation. **T.E. Cocolios:** Writing – review & editing, Investigation, Funding acquisition. **B. Russell:** Writing – review & editing, Methodology, Investigation. **A.J. Fenwick:** Writing – review & editing, Methodology, Investigation. **C. Bernerd:** Investigation. **S. Stegemann:** Writing – review & editing, Investigation. **K. Johnston:** Writing – review & editing, Resources, Project administration, Investigation. **A.M. Gerami:** Investigation. **K. Chrysalidis:** Investigation. **H. Mohamud:** Writing – review & editing, Investigation. **N. Ramirez:** Investigation. **A. Bhaisare:** Investigation. **J. Mewburn-Crook:** Investigation. **D.M. Cullen:** Investigation. **B. Pietras:** Investigation. **S. Pells:** Investigation. **K. Dockx:** Investigation. **N. Stucki:** Investigation. **P.H. Regan:** Writing – review & editing, Supervision.

Declaration of competing interest

The authors declare that they have no known competing financial interests or personal relationships that could have appeared to influence the work reported in this paper.

Data availability

Data will be made available on request.

Acknowledgements

The authors would like to thank Dr Stefaan Pommé for providing the software to perform empirical decomposition. The work performed at NPL was supported by the National Measurements System Programmes Unit of the UK's Department for Science, Innovation and Technology and the European Union's Horizon 2020 research and innovation programme under grant agreement No 101008571 (PRISMAP – The European medical radionuclides programme). P. H. Regan also acknowledges funding from the UK Science and Technologies Facilities Council (grant numbers ST/P005314/1, ST/V001108/1, ST/L005743/1 and ST/P005314). Collections at CERN-ISOLDE were supported by the European Union's H2020 ENSAR2 under grant agreement No 654002 (ENSAR2), FWO-Flanders (Belgium) and KU Leuven STG/15/031.

References

Baum, R.P., Singh, A., Benešová, M., Vermeulen, C., Gnesin, S., Köster, U., Johnston, K., Müller, D., Senftleben, S., Kulkarni, H.R., 2017. Clinical evaluation of the radiolanthanide terbium-152: first-in-human PET/CT with 152 Tb-DOTATOC. Dalton Trans. 46, 14638–14646.

Bé, M.-M., Coursol, N., Duchemin, B., Lagoutine, F., Legrand, J., Debertin, K., Schönfeld, E., 1999. Table de Radionucléides, Introduction. CEA, Saclay, 2-7272-0201-6.

Bé, M.-M., Chisté, V., Dulieu, C., Browne, E., Chechev, V., Kuzmenko, N., Helmer, R., Nichols, A., Schönfeld, E., Dersch, R., 2004. Table of Radionuclides, 2-A= 151 to 242). Monographie BIPM-5.

Bé, M.-M., Chisté, V., Dulieu, C., Mougeot, X., Chechev, V., Kuzmenko, N., Kondev, F., Luca, A., Galan, M., Nichols, A., 2011. Table of Radionuclides, 6–A= 22 to 242). Monographie BIPM-5.

BIPM, 2008. Evaluation of Measurement Data – Guide to the Expression of Uncertainty in Measurement, JCGM100:2008. Bureau International des Poids et Mesures.

Catherall, R., Andreazza, W., Breitenfeldt, M., Dorsival, A., Focker, G., Gharsa, T., Giles, T., Grenard, J., Locci, F., Martins, P., 2017. The ISOLDE facility. J. Phys. G: Nucl. Part. Phys. 44, 094002.

Collins, S.M., Gilligan, C., Pierson, B., Ramirez, N., Goodwin, M., Pearce, A., Archambault, B., Haney, M., Regan, P., 2022a. Determination of the ^{161}Tb half-life. Appl. Radiat. Isot. 182, 110140.

Collins, S.M., Robinson, A.P., Ivanov, P., Köster, U., Cocolios, T.E., Russell, B., Webster, B., Fenwick, A., Duchemin, C., Ramos, J., 2022b. Half-life determination of ^{155}Tb from mass-separated samples produced at CERN-MEDICIS. Appl. Radiat. Isot. 190, 110480.

Collins, S.M., Shearman, R., Ivanov, P., Regan, P., 2020. The impact of high-energy tailing in high-purity germanium gamma-ray spectrometry on the activity determination of ^{224}Ra using the 241.0 keV emission. Appl. Radiat. Isot. 157, 109021.

Cox, M.G., Michotte, C., Pearce, A.K., 2007. Measurement modelling of the International Reference System (SIR) for gamma emitting radionuclides. Monographie BIPM-7..

Dong, J., Bai, T., Hu, Y., Zhang, X., Fan, J., Dai, Y., Miao, L., Yu, X., Li, Z., 2023. Determination of the half-life of ^{161}Tb. Appl. Radiat. Isot. 193, 110647.

Durán, M.T., Juget, F., Nedjadi, Y., Bochud, F., Grundler, P.V., Gracheva, N., Müller, C., Talip, Z., van der Meulen, N.P., Bailat, C., 2020. Determination of ^{161}Tb half-life by three measurement methods. Appl. Radiat. Isot. 159, 109085.

Fenwick, A.J., Collins, S.M., Evans, W.D., Ferreira, K.M., Paisey, S.J., Robinson, A.P., Marshall, C., 2020. Absolute standardisation and determination of the half-life and gamma emission intensities of ^{89}Zr. Appl. Radiat. Isot. 166, 109294.

Gromov, K.Y., Kuznetsov, V., Kuznetsova, M.Y., Finger, M., Urbanec, J., Nielsen, O., Wilsky, K., Skilbreid, O., Jørgensen, M., 1967. The decay of ^{152}Tb. Nucl. Phys. 99, 585–604.

Kossert, K., Takács, M.P., Nähle, O., 2020. Determination of the activity of ^{225}Ac and of the half-lives of 213Po and 225Ac. Appl. Radiat. Isot. 156, 109020.

Köster, U., Fedoseyev, V., Mishin, V., 2003. Resonant laser ionization of radioactive atoms. Spectrochim. Acta B: At. Spectrosc. 58, 1047–1068.

Kuzmenko, N.K., 2019. Updated decay data evaluation for ^{68}Ga. Appl. Radiat. Isot. 152, 188–192.

Martin, M., 2013. Nuclear data sheets for A= 152. Nucl. Data Sheets 114, 1497–1847.

Müller, C., Reber, J., Haller, S., Dorrer, H., Köster, U., Johnston, K., Zhernosekov, K., Turler, A., Schibli, R., 2014. Folate receptor targeted alpha-therapy using terbium-149. Pharmaceuticals 7, 353–365.

Müller, C., Singh, A., Umbricht, C.A., Kulkarni, H.R., Johnston, K., Benešová, M., Senftleben, S., Müller, D., Vermeulen, C., Schibli, R., 2019. Preclinical investigations and first-in-human application of ^{152}Tb-PSMA-617 for PET/CT imaging of prostate cancer. EJNMMI Res. 9, 1–10.

Müller, C., Vermeulen, C., Johnston, K., Köster, U., Schmid, R., Turler, A., van der Meulen, N.P., 2016. Preclinical in vivo application of (152)Tb-DOTANOC: a radiolanthanide for PET imaging. EJNMMI Res. 6, 35.

Müller, C., Zhernosekov, K., Köster, U., Johnston, K., Dorrer, H., Hohn, A., van der Walt, N.T., Turler, A., Schibli, R., 2012. A unique matched quadruplet of terbium radioisotopes for PET and SPECT and for alpha- and beta- radionuclide therapy: an in vivo proof-of-concept study with a new receptor-targeted folate derivative. J. Nucl. Med. 53, 1951–1959.

Nica, N., 2020. Nuclear data sheets for A= 153. Nucl. Data Sheets 170, 1–498.

Pommé, S., Stroh, H., Paepen, J., Van Ammel, R., Marouli, M., Altzitzoglou, T., Hult, M., Kossert, K., Nähle, O., Schrader, H., Juget, F., Bailet, C., Nedjadi, Y., Bochud, F., Buchillier, T., Michotte, C., Courte, S., van Rooy, M.W., van Staden, M.J., Lubbe, J., Simpson, B.R.S., Fazio, A., De Felice, P., Jackson, T.W., Van Wyngaardt, W.M., Reinhard, M.I., Golya, J., Bourke, S., Roy, T., Galea, R., Keightley, J.D., Ferreira, K. M., Collins, S.M., Ceccatelli, A., Unterweger, M., Fitzgerald, R., Bergeron, D.E., Pibida, L., Verheyen, L., Bruggeman, M., Vodenik, B., Korun, M., Chisté, V., Amiot, M.-N., 2016. Evidence against solar influence on nuclear decay constants. Phys. Lett. B 761, 281–286.

Pommé, S., 2015. The uncertainty of the half-life. Metrologia 52, S51–S65.

Pommé, S., De Hauwere, T., 2020. Derivation of an uncertainty propagation factor for half-life determinations. Appl. Radiat. Isot. 158, 109046.

Pommé, S., Pelczar, K., 2021. Empirical decomposition and error propagation of medium-term instabilities in half-life determinations. Metrologia 58, 035012.

Rothe, S., Marsh, B., Mattolat, C., Fedosseev, V., Wendt, K., 2011. A complementary laser system for ISOLDE RILIS. J. Phys.: Conf. Ser. 312, 052020.

Shearman, R., Collins, S.M., Keightley, J.D., Pearce, A.K., Garnier, J., 2017. Absolute intensities of the gamma-ray emissions originating from the electron capture decay of Gd-153. EPJ Web Conf. 146.

Singh, B., 2009. Nuclear data sheets for A = 151. Nucl. Data Sheets 110, 1–264.

Sonzogni, A., 2004. Nuclear data sheets for A= 134. Nucl. Data Sheets 103, 1–182.

Toth, K., Bjørnholm, S., Jørgensen, M., Nielsen, O., Skilbreid, O., Svanheden, Å., 1960. The light terbium isotopes a survey of half-lives and γ-ray spectra with the use of mass-separated samples. J. Inorg. Nucl. Chem. 14, 1–7.

Webster, B., Ivanov, P., Russell, B., Collins, S., Stora, T., Ramos, J.P., Köster, U., Robinson, A.P., Read, D., 2019. Chemical purification of terbium-155 from pseudo-isobaric impurities in a mass separated source produced at CERN. Sci. Rep. 9, 1–9.

Webster, B.L., 2021. The Chemical Separation of Terbium for Applications in Nuclear Medicine. Doctoral dissertation, Univeristy of Surrey.

Zimmerman, B.E., Judge, S., 2007. Traceability in nuclear medicine. Metrologia 44, S127–S132.